Chapter 4

Hypervelocity Microparticle Impact Experiments

4.1 Simulating cosmic dust impacts in the lab: accelerating microparticles

A thorough understanding of the impact ionization process is essential in developing and testing new cosmic dust mass spectrometers, as well as interpreting the results from previous instruments. Controlled studies of impact-related phenomena require the ability to produce high-velocity particles and projectiles in the laboratory. Methods for producing hypervelocity (>1-2 km/s) projectiles began to be developed in the 1950s in both national defense and space-related programs. Defense-related efforts included exploring the possibility of knocking enemy missiles off course by bombardment with large numbers of small, fast particles launched from a satellite [1]. Of concern to the emerging space program was the possibility that spacecraft would suffer damage from continual impacts of dust grains. Another question was whether the lunar surface would be sufficiently solid to land (and relaunch) a manned spacecraft, and whether spacesuits could withstand impacts without being punctured.

In 1955 Fred Whipple and George Gamow recommended that the United States develop three promising methods of producing hypervelocity particles: the light gas gun,

shaped charge jets, and electromagnetic guns [1]. Explosive and magnetic methods were also studied in this context. However, all of these methods had limitations that adversely affected the ability to carefully research the impact phenomenon as it related to microparticles. For instance, each method typically produced numerous hypervelocity particles simultaneously, hindering study of individual impacts. In addition, these methods could not produce particles with velocities greater than approximately 10 km/s.

Direct electrical acceleration of charged particles was also considered for development. A major limitation is that, regardless of the charging mechanism used, particles will all have different mass-to-charge ratios, precluding the possibility of using cyclic or multi-stage accelerators such as synchrotrons or linacs. Charged microparticle acceleration requires a single-stage electrostatic system powered by a very high voltage. For a conducting particle with mass in kilograms, m, and charge in Coulombs, q, accelerated through a voltage, V, the particle kinetic energy is

$$KE = \frac{1}{2}mv^2 = qV \tag{1}$$

and its velocity, in m/s, is

$$v = \sqrt{\frac{2qV}{m}}\,. \tag{2}$$

Of course, the total amount of negative charge on a particle is limited by the electron field emission limit, about 10^9 V/m. The total amount of positive charge on a particle is limited by the ion field emission limit, roughly 10^{10} V/m [2]. The other limiting factor in obtaining high velocities is the availability of high (MV range) voltage sources.

In 1960 Shelton [2] developed and demonstrated an electrostatic accelerator capable of delivering individual, high-velocity, highly charged micron-sized metal particles. Dust particles, such as reduced iron carbonyl, became highly charged upon contact with a charged needle. They were then accelerated through 100 kV. Shelton also constructed a series of induced-charge sensors to measure the velocity and charge of accelerated particles. Friichtenicht [3] used the principles of Shelton's instrument and constructed a larger dust accelerator with a 2 MV van de Graaff accelerator as the voltage supply. Friichtenicht observed particles with velocities as high as 14 km/s. Several other dust accelerators were built at this time—all of them based on Friichtenicht's design [4].

4.2 Impact ionization theory, models, and experiments

In 1964 Friichtenicht [5] observed that hypervelocity impacts of iron particles on metal targets resulted in the production of ions. He found that impacts on metals such as tantalum, tungsten, and platinum produced significantly more ions than impacts on lead, indium, or beryllium-copper. He also found that craters on the former set of metals were much smaller than craters on the latter set of metals, implying a relationship between the ionization susceptibility and cratering susceptibility of the metals. Two directions of research resulted from this discovery: (1) attempts to understand the ion formation process, and (2) efforts to use impact ionization as a method for studying cosmic dust.

Soon after Friichtenicht's discovery Auer and Sitte [6] and Hansen [7] performed nearly identical experiments in which the ions produced during hypervelocity impacts of

iron particles were characterized using time-of-flight mass spectrometry. When extracting positive ions they observed singly charged sodium, potassium, iron, and sometimes hydrogen, carbon, and oxygen. Sodium, although frequently the largest peak in the spectra, constituted only 2 ppm of the target plate composition, as determined using flame photometric measurements. Negative charge extraction experiments showed that electrons accounted for all negative charge produced.

Later experiments by Friichtenicht *et al*. [8], Dietzel *et al*. [9], and Roy [10] showed similar results. From these experiments emerged a theoretical model of impact ionization. Ions from elements with lower ionization potentials (e.g., alkali metals) were much more abundant than ions from elements with higher ionization potentials. The number of ions of each type was consistent, at least to a first approximation, with an equilibrium plasma described by the Saha equation [11]:

$$\frac{n_e n_i^s}{n_n^s} = CT^{3/2}\left(\frac{u_i^s}{u_n^s}\right)e^{\left(\frac{-E_I^s}{kT}\right)}, \tag{3}$$

where n_e is the total number of electrons per unit volume, n_i^s is the number of ions of species *s* per unit volume, n_n^s is the number of neutral species per unit volume, C is a constant, T is the plasma temperature, u_i^s and u_n^s are the internal partition functions of ions and neutrals of species *s*, k is Boltzmann's constant, and E_I^s is the ionization potential of species s. The presence of certain species with high ionization potentials, such as hydrogen, carbon, and oxygen, was much greater than could be accounted for in this equilibrium plasma model. However, the intensities of hydrogen, carbon, and oxygen peaks increased with impact velocity. Friichtenicht [8] and Roy [10] used the ratios of ions of metal species (including alkali metals) to estimate the plasma

temperatures in impacts, which they reported as being typically 6000 K ± 3000 K for impacts in the range of 20-50 km/s. Their data show no relationship between plasma temperature and impact velocity within this range of velocities, although such a relationship was expected. In each of these studies the total charge, Q, produced during an impact was fit to the empirical relationship:

$$Q = Km_p^{\alpha} v^{\beta}, \tag{4}$$

where K is a constant for each material (dependent largely on the atomic mass), m_p is the mass of the particle, and v is the impact velocity. Values for α range from 1.33 to 0.154 and seem to show a dependence on both the impact velocity and the experimental conditions. The value of β is usually near 1.

In the 1980s three identical impact ionization time-of-flight mass spectrometers were included on three of the five spacecraft that encountered Halley's Comet [12]. During this time, laboratory dust impact experiments focused on the goal of understanding impacts in the velocity range of the comet encounter, 70-80 km/s. No new results were obtained, but a great deal of work was done in comparing impact ionization yields to other ionization types, such as ion or atom bombardment, IR and UV laser ionization, and electronic ionization [13, 14]. Data from the comet particles showed an unexpectedly large number of hydrogen (H), carbon (C), nitrogen (N), and oxygen O) ions [15, 16], as well as expected ions from iron, silicon, and magnesium [17]. The lighter elements, H, C, N, and O, were interpreted to indicate the presence of relatively high concentrations of organic species, supported by the presence of very small peaks at heavier masses corresponding possibly to organic fragments and molecules [18, 19].

More recent contributions to understanding impact ionization have included hydrocode calculations and other theoretical treatments [20-22] that estimate ionization parameters based on shock wave propagation and the thermodynamic properties of irreversible adiabatic expansions. However, these calculations are unable to explain the presence of many ions for impacts at less than 40 km/s, and they greatly underestimate the ion yield of species such as hydrogen, carbon, and oxygen. They attributed these "extra ions" to surface disturbances, as occur when a shock wave reaches a free surface. Recent experiments [23] also show ions assumed to be produced in an equilibrium plasma with unexplained ions such as hydrogen, carbon, nitrogen, or oxygen.

In 1991 Abramov and co-workers [24] examined the angular and energy distributions of ions produced in impacts of aluminum particles with velocities of 1-11 km/s, although results are only presented for a particle with a velocity of 3.4 km/s. In this case the initial kinetic energies were on the order of 2 eV. They note, however, that these ions were extracted using a very low electric field (1 V/cm), and that higher fields produced larger kinetic energies. Their energy analysis was based on the widths of the mass spectra peaks, although no information about calibration was given.

In the latter half of the 1990s, researchers at the University of Kent at Canterbury, England, performed several dust accelerator experiments in order to determine the nature of the ionization mechanism and ion yields for different species. Comparing experimental results to theoretical predictions shows good agreement for metal ions but poor agreement for non-metal ions [25]. However, theoretical predictions using different methods sometimes vary considerably. In one experiment they observed the shape of the mass spectra peaks for ions originating from a 94 km/s impact of a

boron carbide particle on a silver-doped aluminum surface [26]. They observed peaks corresponding to hydrogen, carbon, aluminum, and silver. Although only one spectrum was observed, they used the shapes of each spectral peak to estimate the thermal properties of the ions produced. They reported that both hydrogen and carbon ions were best fit by a Gaussian curve, indicating a non-equilibrium plasma. Hydrogen ions had an initial kinetic energy of 160 ± 16 eV, while carbon ions were 40 ± 25 eV. Aluminum ions showed initial kinetic energies of 9.7 eV, and the peak shape was not easily fit to either a Gaussian or Maxwellian curve, so no distribution was given. Hydrogen ions showed an angular distribution of $\cos^3 \theta$ with respect to the normal, while aluminum ions showed a $\cos^2 \theta$ distribution. They note that the number of carbon ions detected was greater than the number of carbon atoms assumed to be present in the impacting boron carbide particle. Presumably both hydrogen and carbon had come from some other source, such as pump oil adsorbed to the exterior of the particle and aluminum surface. Of course, if sufficient oil had adsorbed onto the particle to produce as many ions as they saw, the particle's velocity would have been greatly reduced before striking the impact plate of their mass spectrometer. The initial kinetic energies of ions produced showed a large variation, revealing a complication in the traditional impact ionization mechanism. Not only were hydrogen and carbon ions being produced in much greater quantities than theory predicted, but they were being produced with larger initial kinetic energies than expected.

Although the energy required to produce free H^+, C^+, and O^+ is much higher than the impact energy, their presence may be explained by a theory proposed by Novikov [27] and discussed by Sysoev [28, 29] and McDonnell [30]. They postulate that an electric

discharge occurs between the charged particle and target surface immediately before impact. According to their model, as the charged microparticle approaches the surface, the high electric field causes electrons to be emitted from the target surface and strike the particle, causing electron-induced desorption and ionization. Implications of this model are discussed in greater detail in Section 4.8. Of particular importance are implications of charge-induced ionization on interpretation of the spectra taken during hypervelocity microparticle impact studies of the Dustbuster. Of course, this mechanism also has implications for interpretation of spectra from other instruments, and this is also discussed.

4.3 The dust accelerator at Concordia College, Moorhead, Minnesota

Following laser desorption experiments (described in Chapter 3), the Dustbuster was tested using hypervelocity microparticle impacts to simulate cosmic dust. These tests were conducted on the van de Graaff dust accelerator at Concordia College in Moorhead, Minnesota.

One of the original Friichtenicht-style dust accelerators was built for NASA in the early 1960s under the direction of Otto Berg. When funding for dust research became sparse, use of this accelerator was discontinued, and in 1975 the accelerator was donated to Concordia College, Berg's *alma mater*. The faculty of the Concordia Physics Department has maintained the accelerator in working condition since then. To my knowledge it is now the only operational van de Graaff dust accelerator in the Western Hemisphere (other operational accelerators being in Germany and England, and a

recently constructed accelerator in Japan). Hypervelocity microparticles produced at the Concordia dust accelerator were used for testing the Dustbuster and for other microparticle impact studies.

The design of the Concordia dust accelerator is essentially identical to Friichtenicht's accelerator [3], and is shown in Figure 4.1. The principal components include the vacuum system, the dust reservoir and charging needle, the 2 MV van de Graaff ball, and charge-sensitive electrodes along the length of the flight tube.

The dust reservoir and charging needle, illustrated in Figure 4.2, are located within the van de Graaff ball. Because the dust reservoir is floated at high voltage, all the associated electronics are optically isolated. The dust particles, typically a fine powder (particle sizes ranging from about 0.1 to 10 μm) are stored in a small box-like cavity. Above the powder rests a planar electrode (the "tongue"), normally at the same electrical potential as the dust. When the dust source is triggered, a voltage is applied to the tongue, creating an electric field in the box and inducing charge on the dust grains. If the Coulombic repulsion on a given grain is sufficient to overcome gravity, the particle rises and strikes the tongue. The resulting dust motion is similar to the motion of gas molecules. Eventually some dust grains will leave the dust reservoir through a small hole and enter the region of the charging electrode. In this region particles continue to "bounce around," acquiring the potential of the surface contacted. Due to this random motion, particles may come into contact with the charging electrode, which is held at a potential several kV higher than the surroundings. Upon contact with the charging electrode, particles acquire a large positive charge, and some of them may have

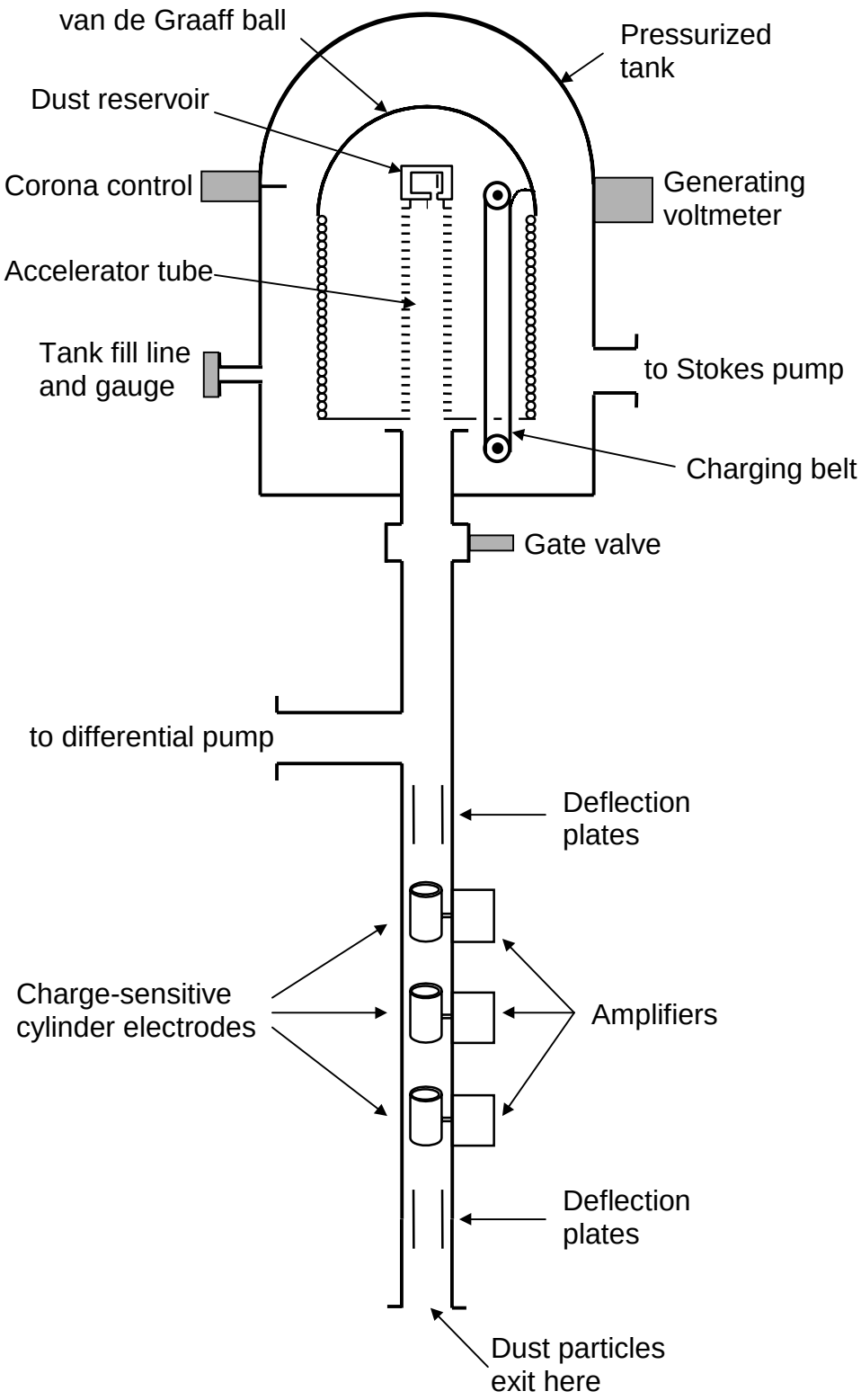

Figure 4.1. Diagram of the van de Graaff dust accelerator at Concordia College.

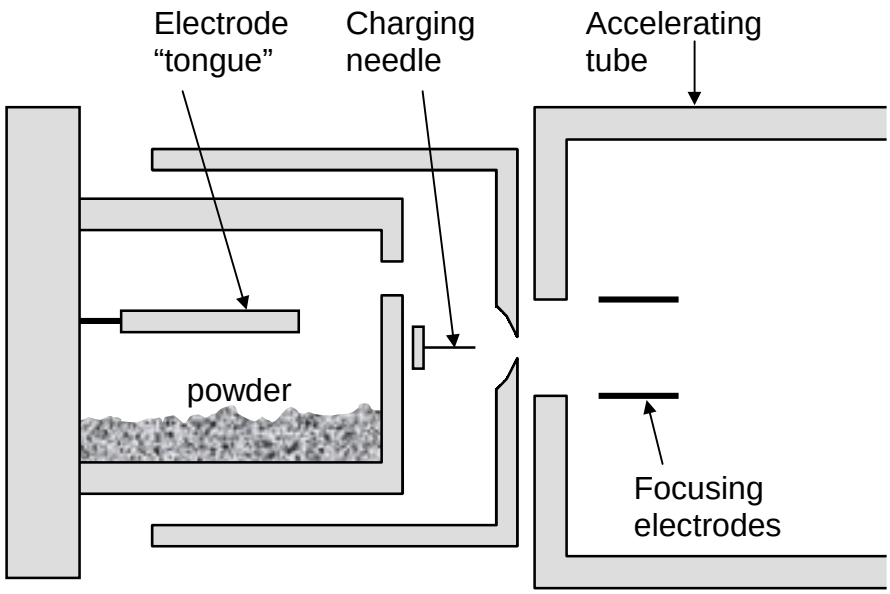

Figure 4.2. Details of the dust reservoir of the van de Graaff accelerator.

the proper trajectory to leave the charging region and enter the accelerating tube. In the accelerating tube particles are accelerated from the van de Graaff voltage to ground.

Three cylindrical electrodes within the flight tube allow measurement of the charges and velocities of the accelerated particles. Each particle induces an image current as it passes through each cylinder. The resulting voltage pulses are combined, amplified, and recorded by an oscilloscope. Particle charge, q, can then be calculated using the relation

$$q = CV \,, \tag{5}$$

where C is the measured capacitance of the first cylinder electrode in the drift tube, and V is the magnitude of the induced voltage pulse. Particle velocity is determined from the distance between the other two electrodes and the time between those signals. Particle mass, m, is found from

$$m = \frac{2qV_a}{v^2} \,, \tag{6}$$

where V_a is the total accelerating voltage and v is the measured particle velocity. The lower limit of charge sensitivity of the cylinder electrodes is around 1 fC, corresponding to a maximum observable velocity of 20-30 km/s and minimum observable mass of around 5×10^{-18} kg, based on typical surface charge densities of the accelerated metal particles. Charge is roughly proportional to surface area and mass is proportional to volume, leading to an overall $v \propto r^{-1/2}$ relationship. As a result, smaller particles with less charge are accelerated to higher velocities than larger particles with more charge. Although the van de Graaff ball is rated at 2 MV, due to various limitations the ball is routinely used at only 1.5 MV.

The flight tube also has several electrodes used to select particles with mass and velocity that fall within specified limits, and deflect particles outside those limits. Although these plates could be used for beam alignment, they typically are not. The accelerator is also equipped with a delayed trigger system, in which a trigger pulse is produced when the particle reaches some point beyond the flight tube.

4.4 Characterization of microparticle impacts using energy analyzer

In order to better understand the impact ionization process, I designed and built a pulsed ion energy analyzer to examine the initial kinetic energies of microparticles accelerated with the Concordia accelerator. Ideally an energy analyzer for this purpose would measure both the kinetic energy distribution and the spatial distribution of each type of ion. Most energy analyzers, such as retarding field [31], cylindrical mirror [32], and directional filtering analyzers [33] require a continual beam of ions, and the energy or spatial distribution is scanned in some fashion. Pulsed ion sources cannot be scanned, although statistical analysis of many pulses can be used to give similar results. Pulsed ion sources are generally studied using time-of-flight methods [34]. In time-of-flight methods, the arrival time of any given ion is related to its initial kinetic energy (plus any additional extraction energy). Analysis of ion energies is subject to errors due to the same factors that affect mass resolution, including detector response, space-charge effects, and ion optics problems [35]. The time-of-flight method was used by Ratcliff for analysis of the 94 km/s impact [26] and by Abramov for lower velocity impacts [24]. In designing my energy analyzer I was severely limited both by time and money. Rather

than performing a fitting analysis on peak shapes as Ratcliff had done, I designed and built a novel pulsed ion energy analyzer based on spatial filtering of ions.

The design of the impact ionization energy analyzer is shown in Figure 4.3. Accelerated dust particles impact the target plate, which is held at some potential. Ions from the impact are extracted by a grounded grid, pass through a reflectron, and are focused onto a microchannel plate detector. However, as the ions leave the reflectron, two removable rings block most of the ions from reaching the detector. The only ions that reach the detector are those for which the velocity components perpendicular to the instrument axis fall within some range. Thus only a "ring" of ions is permitted into the drift region. Varying the extraction voltage and varying the radius of the rings between impacts allows ion energies to be "scanned." Of course, for a given particle, only one range of energies can be detected. Forming a complete distribution description requires a statistical analysis of ions from numerous impacts. While most energy analyzers measure only the "component of kinetic energy" perpendicular to the surface at which ions are formed, this energy analyzer measures the component parallel to the surface (and perpendicular to the instrument axis). Additionally, if the voltage of the front grid is close to the extraction voltage, ions with perpendicular energy components greater than that difference escape the instrument, and are not detected. Thus it is also possible, at least in theory, to scan the perpendicular component of energy, similar to a retarding field analyzer, but subject to the previously mentioned statistical limitations of a pulsed ion source.

The components of energy (or more correctly, velocity) parallel to the impact surface are the result of several factors. First, of course, is the thermal energy and

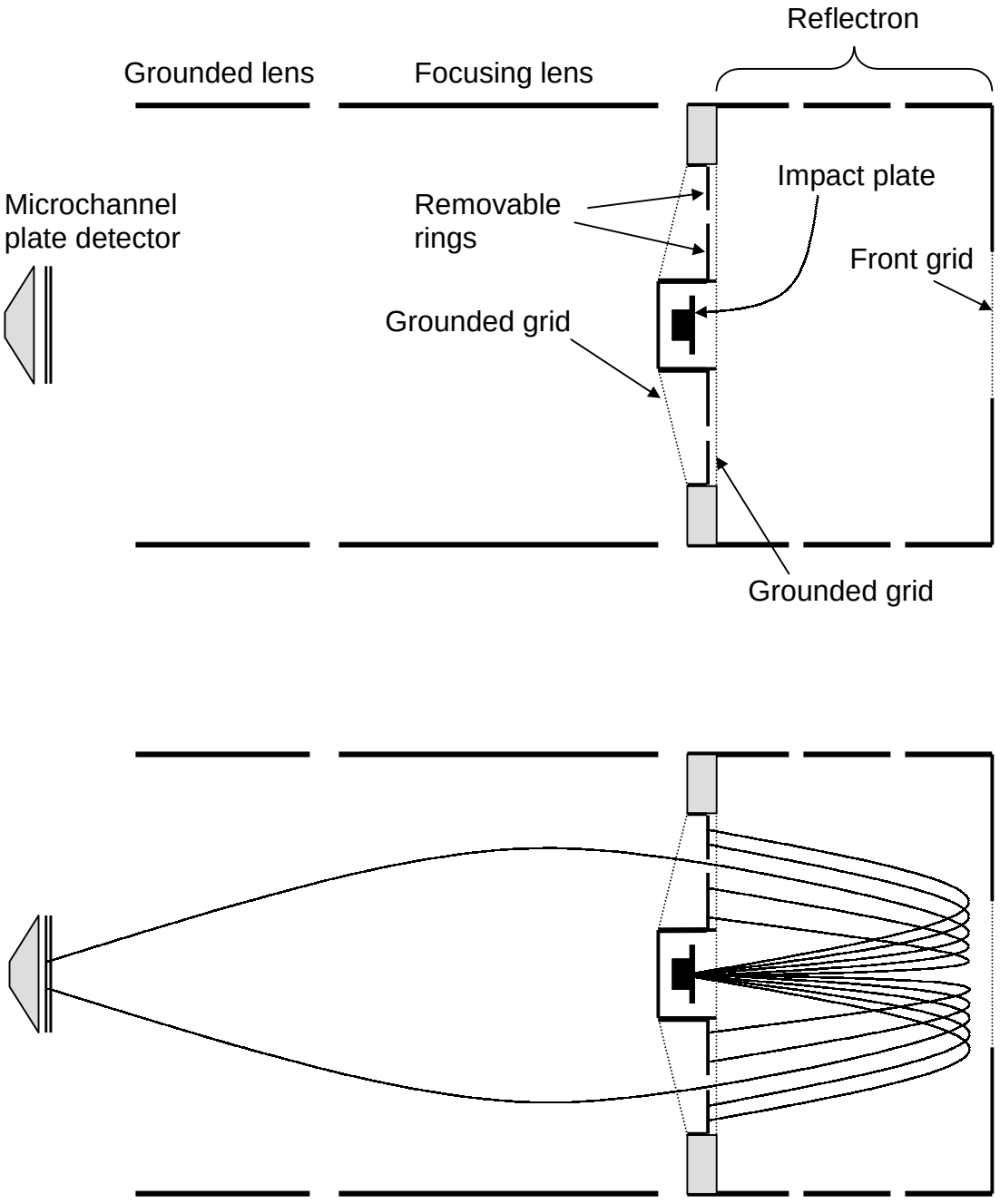

Figure 4.3. Diagram of the energy analyzer. Ions are created at the impact plate, extracted into the reflectron region, and selected for energy at the exit of the reflectron. Ions with correct energies pass on to the MCP detector. In the lower diagram typical ion paths are shown.

spatial distribution arising from the impact plasma itself. Related to this are space-charge effects, which still apply after the plasma expands to a collisionless state. Third, impacts plasmas may not be symmetrical. Spatial inhomogeneities may lead to different local plasma pressures, and ions emerging from these regions may have exceptional kinetic energies. Fourth, although ions are extracted by a reasonably uniform electric field, grid scatter increases the beam spread and increases the average velocity components in these two directions. Lastly, the large electrical field in the extraction region may have an effect on ion energies other than simple addition. Although only the first of these effects is of interest to impact ionization theory, all five factors will be operative in any cosmic dust time-of-flight mass spectrometer. Thus the results from the energy analyzer represent actual conditions in real instruments. Other small effects may influence the spreading out of the ion packet as it traverses the reflectron. These include off-center impacts, roughness of the impact surface, grid scatter from the front grid, imperfect machining and assembly, or inhomogeneous electrical fields in the ion extraction and reflectron regions. It is difficult to assess the relative importance of these factors, and no attempt was made to do so.

Performance of the energy analyzer was simulated using SIMION ion trajectory software. Figure 4.4 shows a typical case.

Figure 4.5 shows the experimental setup for hypervelocity impact studies using the energy analyzer. A mixture of micron-sized iron and copper particles were placed in the dust reservoir. The dust reservoir ball, chamber, and flight tube were then evacuated. On average, 1-10 particles per minute struck the energy analyzer impact plate.

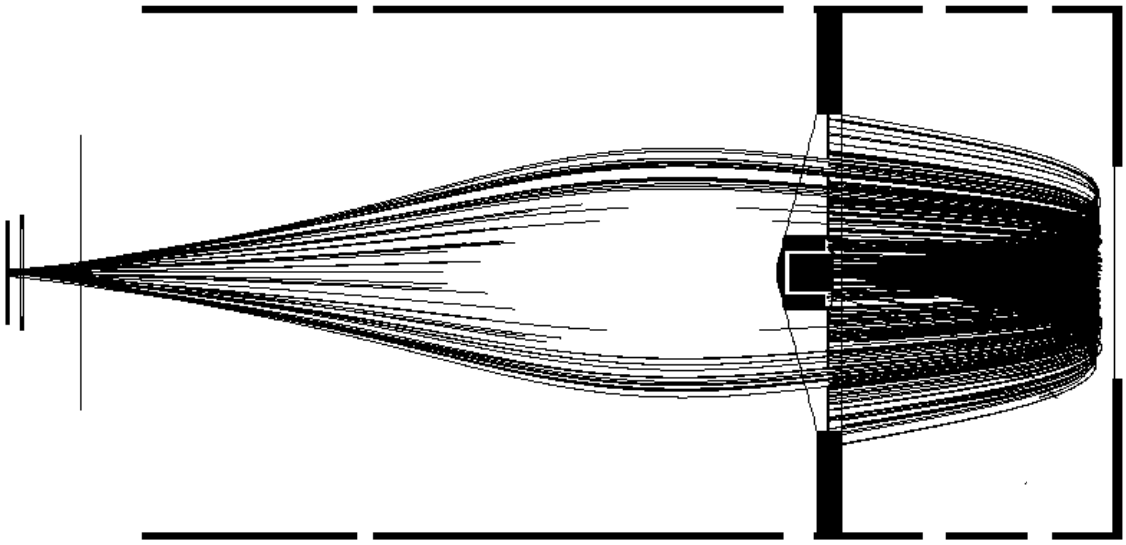

Figure 4.4. Simulation of ion trajectories in the energy analyzer. This is a cut-away view, so portions of the ion trajectories disappear if they are too far away from the plane. Ions have initial KE of 40 eV +/- 25 eV. Extraction voltage is 2600 V, and the opening between rings is at an intermediate radius, as shown.

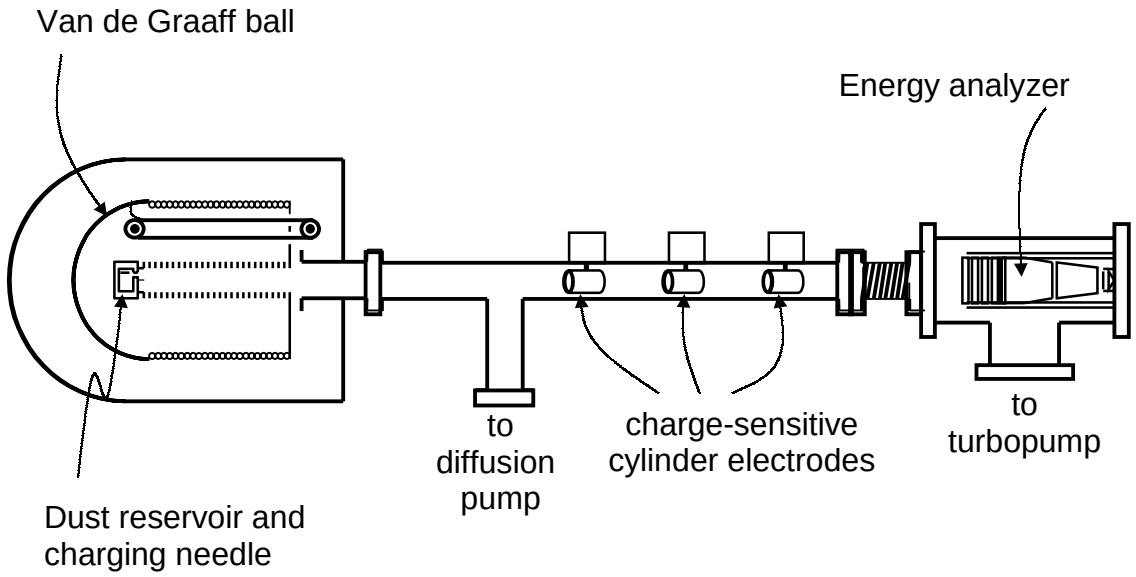

Figure 4.5. Experimental setup for energy analyzer experiments on Concordia van de Graaff dust accelerator. Particles are charged within the van de Graaff ball, then accelerated onto the energy analyzer. Cylindrical electrodes within the flight tube measure charge and velocity of accelerated particles.

The dust reservoir, accelerator, and flight tube were evacuated by a diffusion pump. Because this vacuum system was only able to maintain 3×10^{-6} torr at the exit of the flight tube, the energy analyzer was mounted inside its own vacuum chamber, evacuated by a turbopump to 10^{-7} torr. The two vacuum systems were connected with a 1-cm circular aperture, through which the charged particles left the flight tube and entered the energy analyzer. A flexible bellows allowed alignment of the particle beam (which had a typical spread of 2 mm) with the energy analyzer impact plate.

Particles used included wire-exploded copper with an average diameter of 100-150 nm (Argonide Nanomaterials), 1-micron copper (Sigma Chemical), and 0.1- to 3-micron (diameter) iron spheres produced by the mist reduction of iron carbonyl (General Aniline and Film Corp.).

Spectra were recorded using a 150 MHz Yokagawa digital oscilloscope, which was triggered by the signal on the MCP detector. Over 1,000 dust impact spectra were recorded. Target plate composition included tantalum and molybdenum. Extraction voltages ranged from 150 to 4800 V. The distance between the impact plate and extraction grid was varied between 4, 8, and 12 mm in order to observe any plasma shielding effects. Combinations of any two of ten rings allowed different radii for allowed ions to pass. Unfortunately, interchanging rings, changing the physical length of the extraction region, and changing the impact plate material required breaking vacuum, so a total of only six combinations were used. The ring sizes were chosen to detect ions with energies up to 50 eV (again, referring to the total magnitude of the energy components parallel to the impact plate). It was assumed that for impacts in the range of 1-10 km/s essentially all ions would have less kinetic energy than this. The

energy analyzer was not designed with the capability of measuring the angular or spatial distribution of ions, nor did it have a way of distinguishing a spatial distribution function from the energy distribution function. On the other hand, the entire instrument was designed and built in only two weeks, and at a cost (for materials) of less than $50.

4.5 Results of pulsed ion energy analyzer experiments

Figure 4.6 shows several spectra typical of those acquired on the energy analyzer. Peaks frequently appearing include hydrogen, carbon, oxygen, sodium, potassium, iron, copper, and tantalum. These peaks are the same as those observed in previous impact experiments [10]. Molybdenum appeared in some spectra in which particles impacted the molybdenum plate. A discussion of the origins of each of these peaks is given in Section 4.7.

Variables taken into account in the data analysis included particle velocity, mass, composition, target material, extraction voltage, ring radii, and detector gain. Because of the large number of variables involved, and the large variations between spectra from otherwise identical impacts, no statistically significant information was obtainable regarding the energy distribution of ions produced. However, one interesting and important observation was made: even with the highest extraction voltage (4800 V) and the largest ring set, a large number of ions were still reaching the detector, even for slow impacts (2-3 km/s). This implies that the initial kinetic energy components parallel to the impact surface were quite high for these impacts. The ions resulting from these impacts had initial kinetic energies of at least 50 eV, and probably much higher.

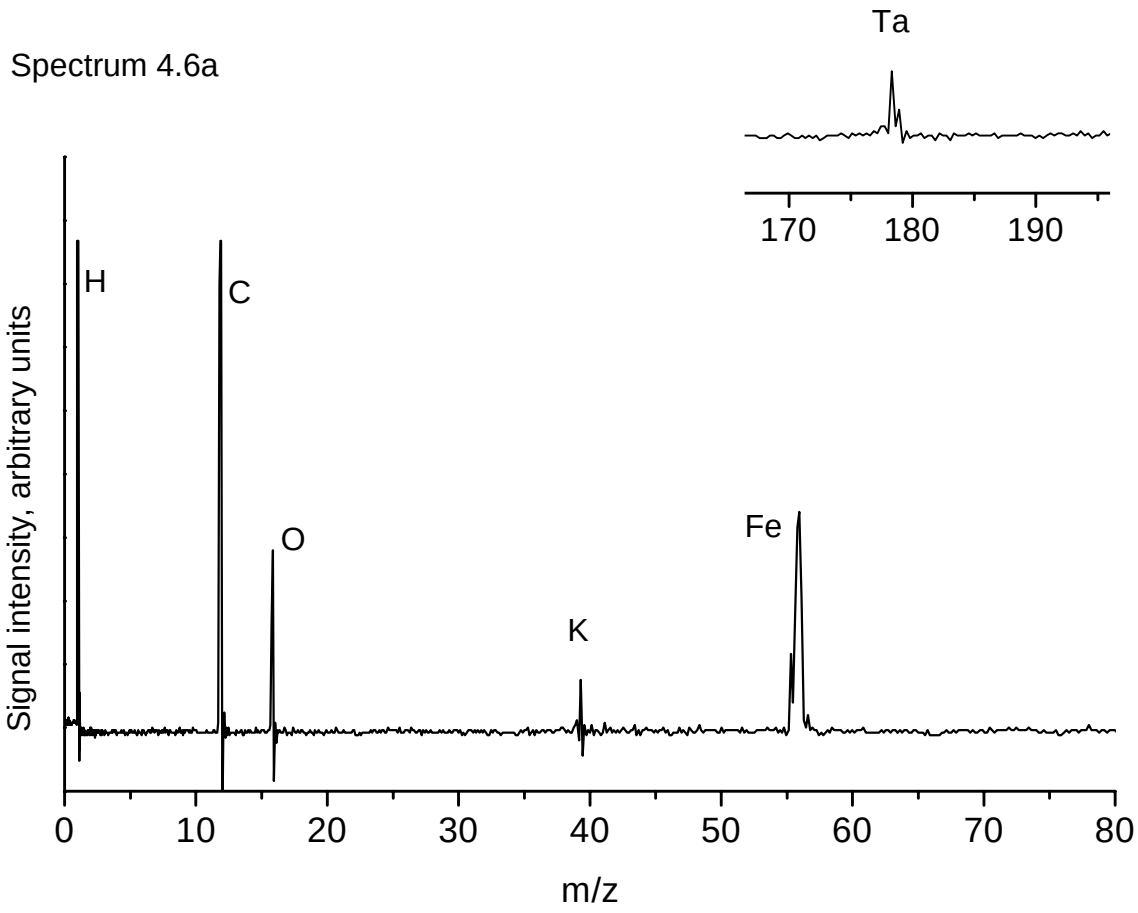

Figure 4.6. Typical spectra from energy analyzer. Spectrum 4.6a is from a 1.88×10^{-15} kg iron particle impacting the tantalum target at 3.3 km/s. Extraction voltage: 4750 V, extraction region length: 12 mm, ring set: 0.73-0.88" radius, MCP detector: ~767 volts per plate.

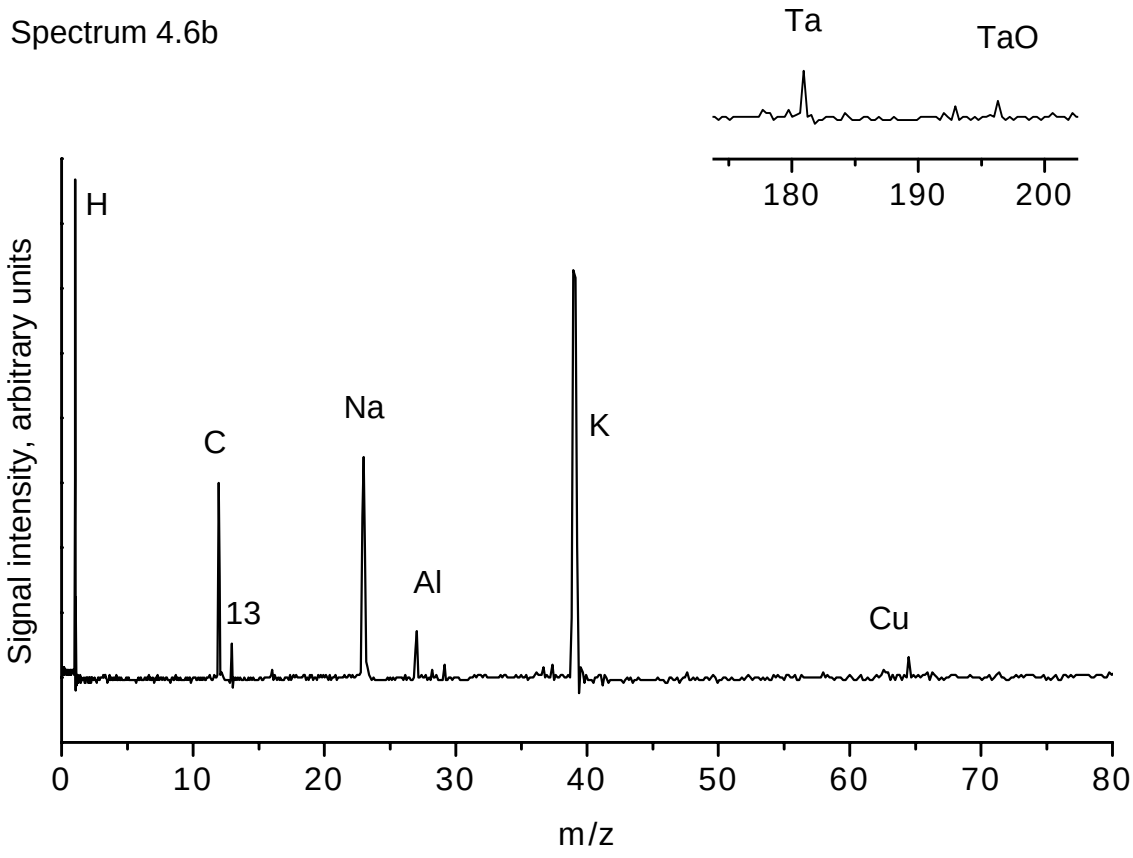

Figure 4.6, continued. Typical spectra from energy analyzer. Spectrum 4.6b is from a 3.37×10^{-16} kg copper particle impacting the tantalum target at 6.4 km/s. Extraction voltage: 4750 V, extraction region length: 12 mm, ring set: 0.73-0.88" radius, MCP detector: ~767 volts per plate.

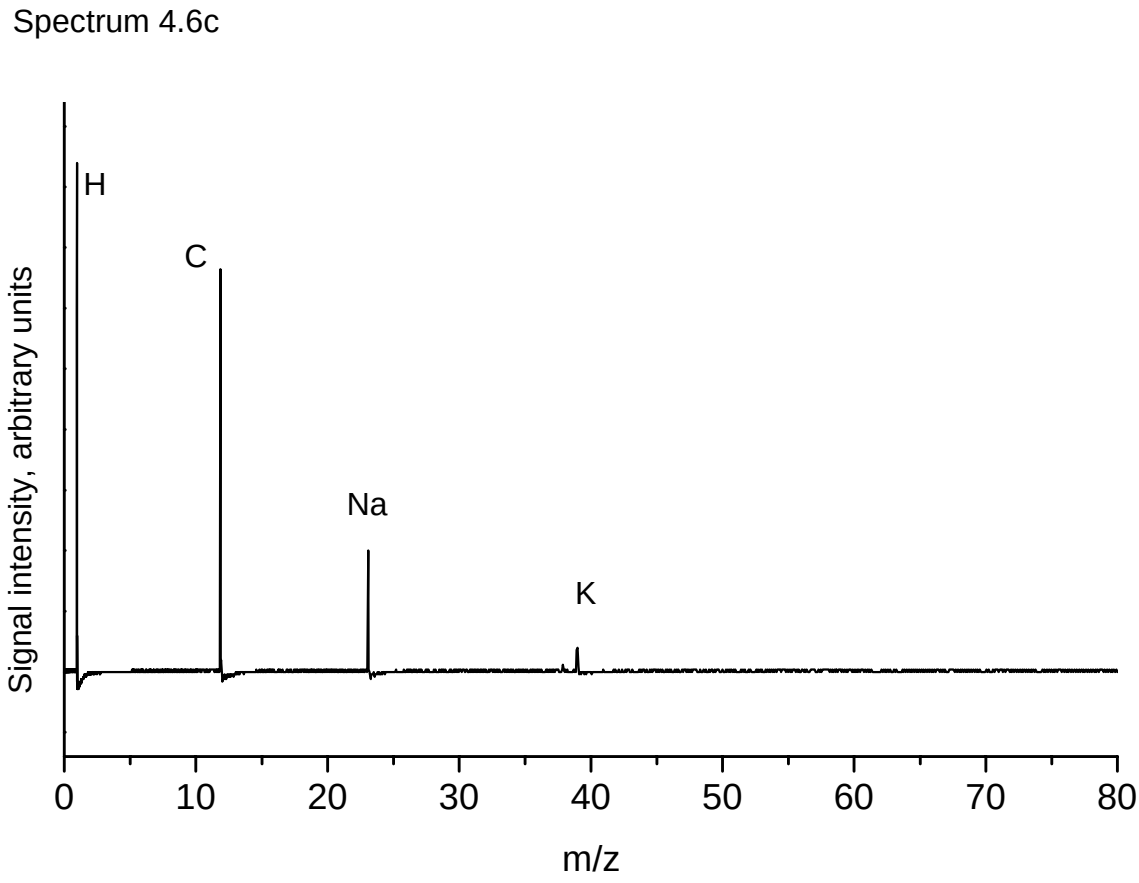

Figure 4.6, continued. Typical spectra from energy analyzer. Spectrum 4.6c is from an impacting particle with unknown mass and velocity. Extraction voltage: 950 V, extraction region length: 9 mm, ring set: 0.50-0.66" radius, MCP detector: ~833 volts per plate.

Spectrum 4.6d

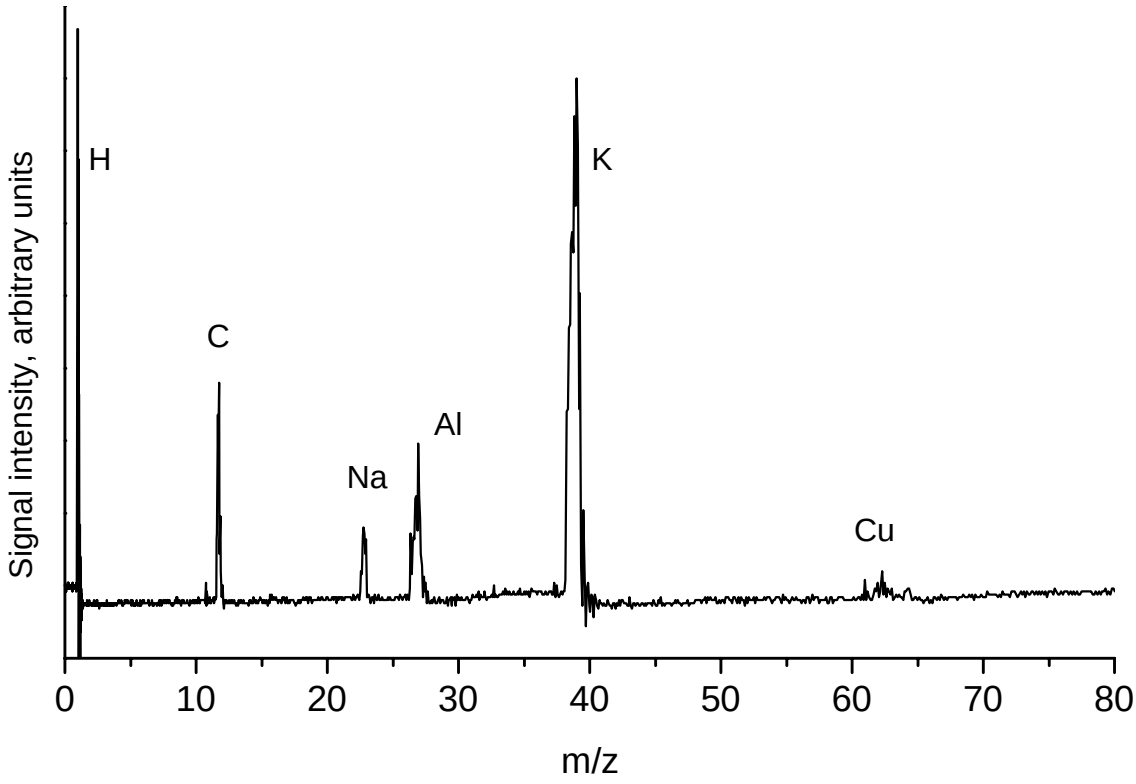

Figure 4.6, continued. Typical spectra from energy analyzer. Spectrum 4.6d is from an impacting copper particle with unknown mass and velocity. Extraction voltage: 1925 V, extraction region length: 9 mm, ring set: 1.09-1.25" radius, MCP detector: ~767 volts per plate.

Spectrum 4.6e

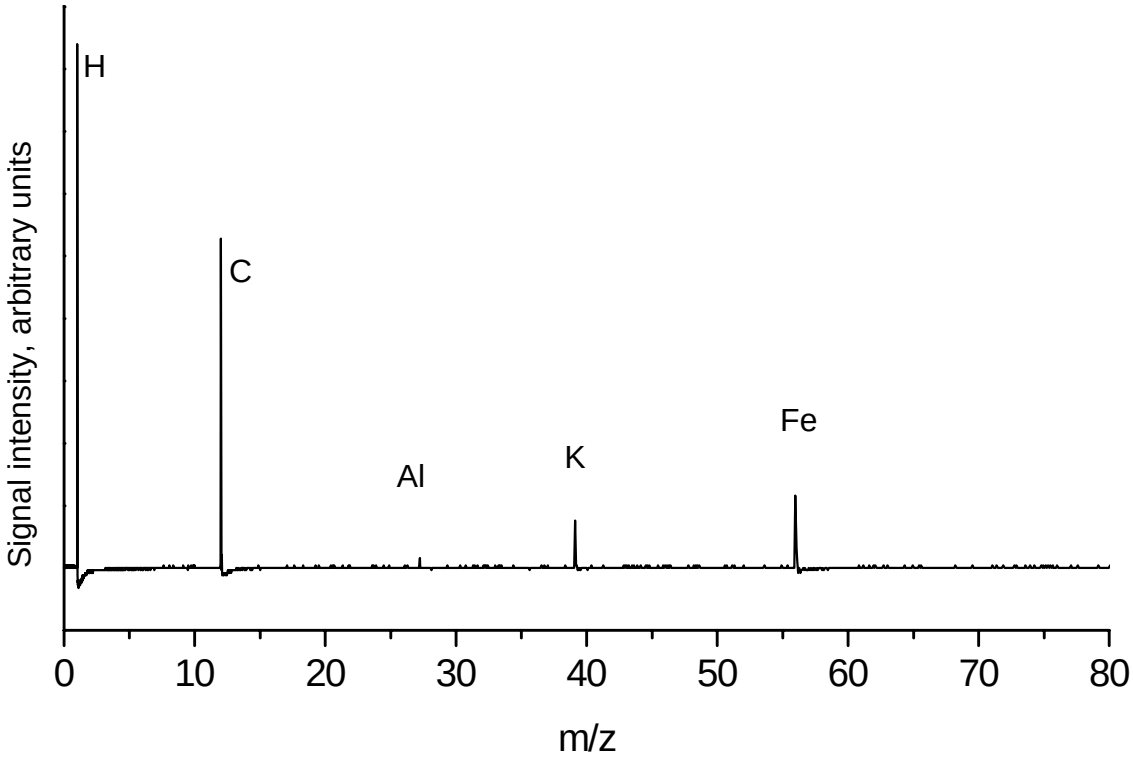

Figure 4.6, continued. Typical spectra from energy analyzer. Spectrum 4.6e is from an impacting iron particle with unknown mass and velocity. Extraction voltage: 950 V, extraction region length: 9 mm, ring set: 0.50-0.66" radius, MCP detector: ~833 volts per plate.

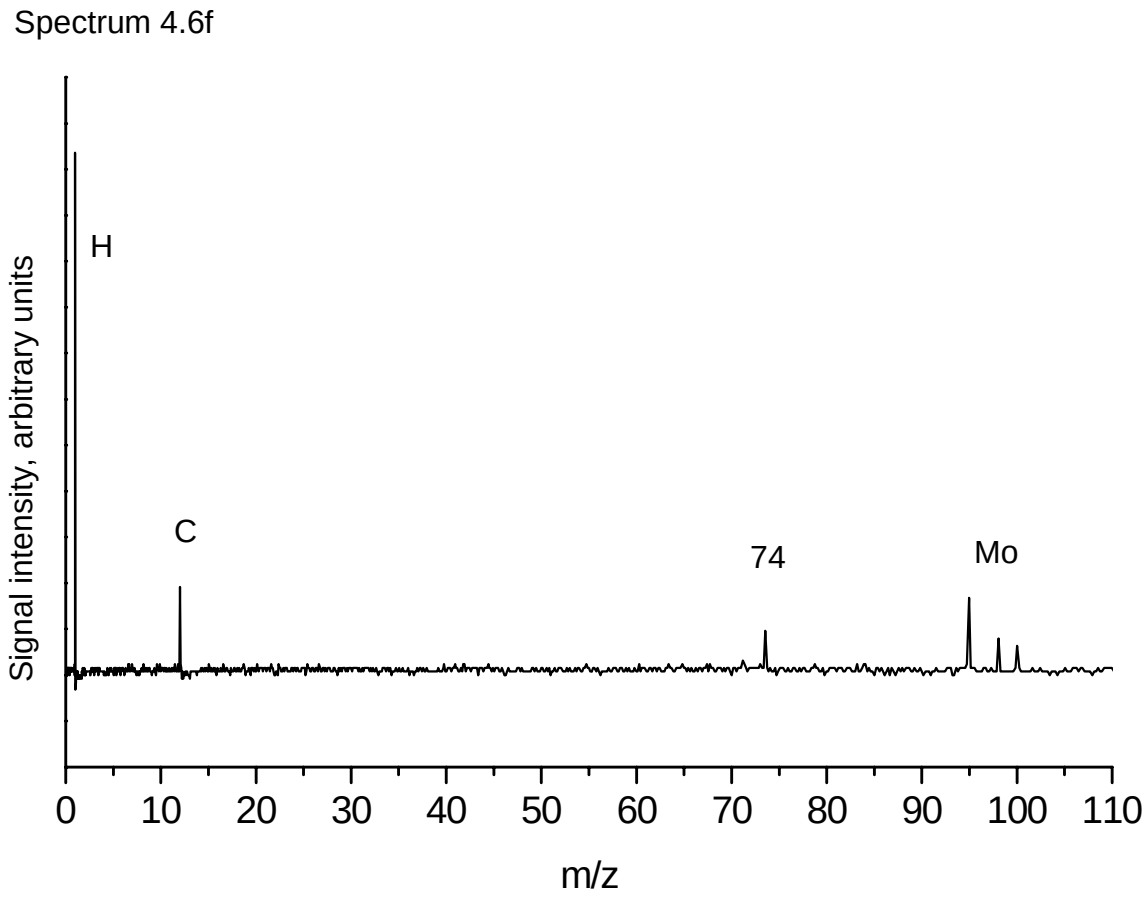

Figure 4.6, continued. Typical spectra from energy analyzer. Spectrum 4.6f is from an impact on the molybdenum target plate by 3.3 km/s, 1.6×10^{-14} kg particle. Three isotopes of molybdenum are clearly visible (95, 98, and 100); other isotopes do not appear. Extraction voltage: 3800 V, extraction region length: 9 mm, ring set: 0.73-0.88" radius, MCP detector: ~833 volts per plate.

Spectrum 4.6g

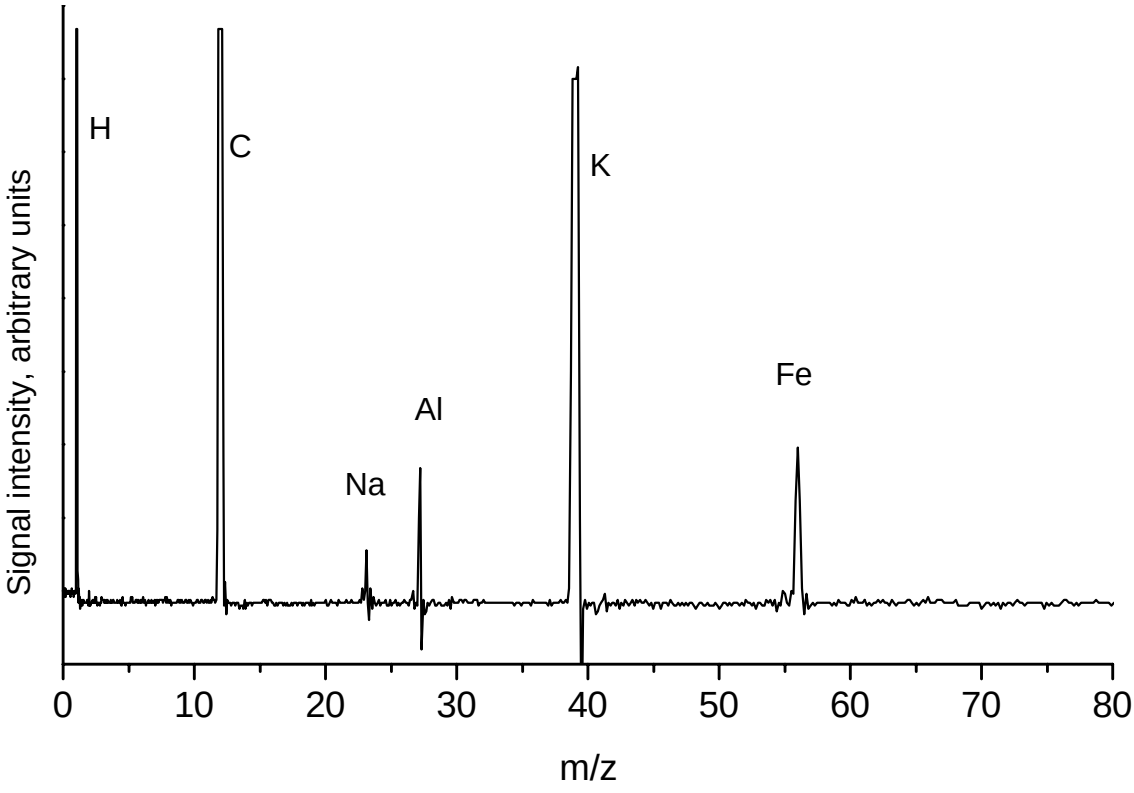

Figure 4.6, continued. Typical spectra from energy analyzer. Spectrum 4.6g is from an impacting iron particle with unknown mass and velocity. Extraction voltage: 4500 V, extraction region length: 9 mm, ring set: 1.09-1.25" radius, MCP detector: ~767 volts per plate.

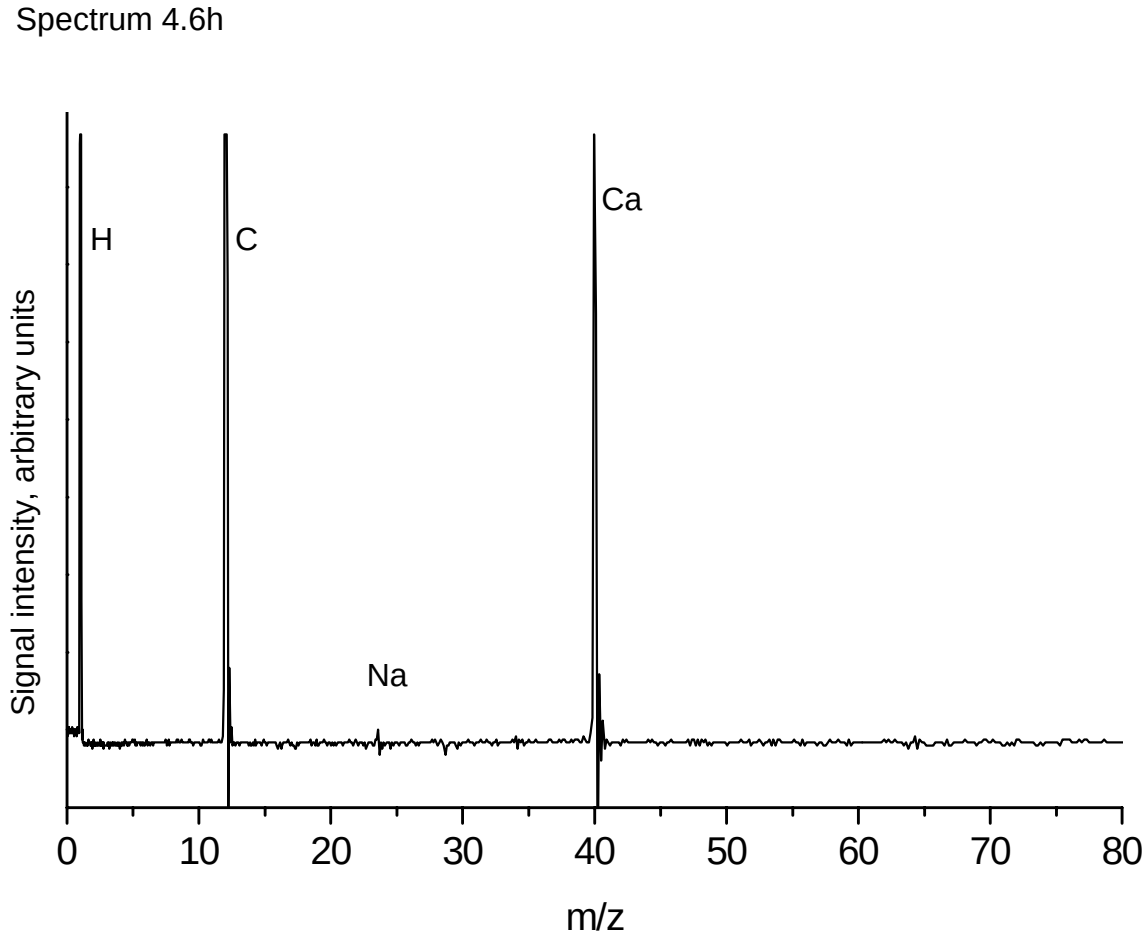

Figure 4.6, continued. Typical spectra from energy analyzer. Spectrum 4.6g is from an impacting particle with unknown mass and velocity. Extraction voltage: 4500 V, extraction region length: 9 mm, ring set: 1.09-1.25" radius, MCP detector: ~767 volts per plate.

Although some of this detected kinetic energy may be due to grid scatter effects, such effects will be present in the Dustbuster and other dust mass spectrometers, and must be taken into account when designing ion optics systems for such instruments. Effects of grid scatter and related extraction phenomena on initial kinetic energies would not have appeared in the experiments of Abramov [24]. Some contribution to the initial kinetic energies undoubtedly came from the thermal properties of the plasma, although separating these two types of effects is not possible at this time. The large initial kinetic energies are not explainable using models of shock-induced ionization and equilibrium plasma. They may be the result of more highly energetic (although perhaps more localized) ionization effects.

4.6 Experimental setup for Dustbuster testing

Hypervelocity microparticles from the Concordia dust accelerator were also used to test the performance of the Dustbuster.

The experimental setup was similar to that used with the energy analyzer, as illustrated in Figure 4.7. Micron-sized iron and copper particles were placed in the dust reservoir. The dust reservoir ball chamber and flight tube were then evacuated. On average, 1-10 particles per minute struck the Dustbuster impact plate. Because the spectrum acquisition time was only 10 μs, the probability of overlapping spectra from coincident particles was negligible.

The dust reservoir, accelerator, and flight tube were evacuated by a diffusion pump. Because this vacuum system was only able to maintain 3×10^{-6} torr at the exit of

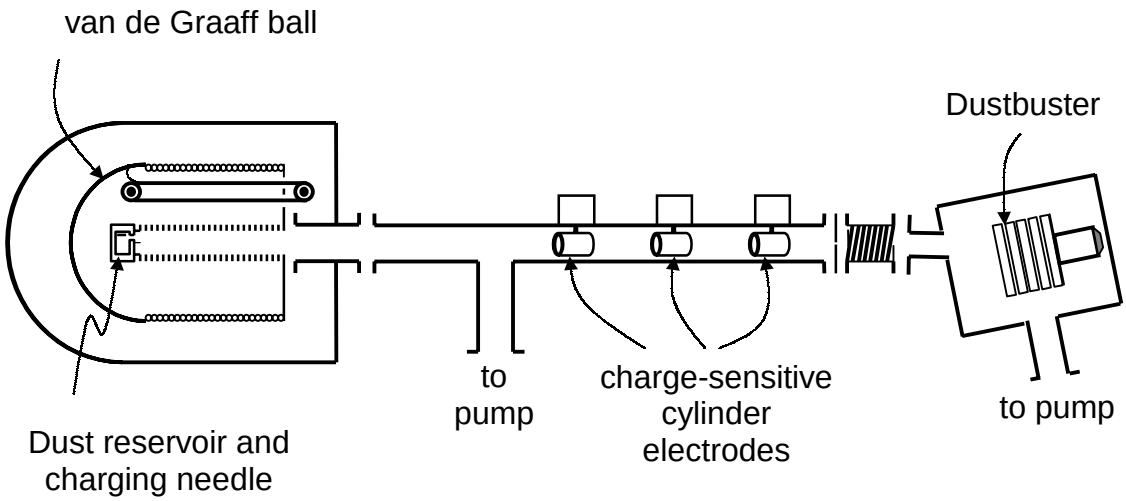

Figure 4.7. Experimental setup for particle impact studies on the Dustbuster. Particles are charged within the van de Graaff ball, then accelerated onto the Dustbuster target plate. Cylindrical electrodes within the flight tube measure charge and velocity of accelerated particles. To permit alignment and testing, the entire Dustbuster vacuum chamber is mounted on a translation/rotation stage capable of motion in all six degrees of freedom.

the flight tube, the Dustbuster was mounted inside its own vacuum chamber, evacuated by a turbopump to 10^{-7} torr. The two vacuum systems were connected with a 1-cm circular aperture, through which the charged particles left the flight tube and entered the Dustbuster. The Dustbuster vacuum chamber included angled connection ports in order to observe particle impacts at angles of up to 25° from the normal. Further, a flexible bellows directed the particle beam to various locations on the target plate, covering all radial distances from 1.5 to 4 cm from the instrument axis. The Dustbuster vacuum chamber was mounted on a large, custom-designed xyz translation/3-axis rotation stage which assisted in varying and measuring the angle and location of the particle impacts on the target plate.

Particles used included wire-exploded copper with an average diameter of 100-150 nm (Argonide Nanomaterials), 1-micron copper (Sigma Chemical), and 0.1- to 3-micron (diameter) iron spheres produced by the mist reduction of iron carbonyl (General Aniline and Film Corp.). The majority of experiments were carried out using iron particles alone. On the assumption that the composition of each particle could be deduced from its mass spectrum, the dust reservoir was filled with a mixture of copper and iron powder in a few later experiments.

For these experiments the entrance grid and extraction grid of the Dustbuster were made of knitted tungsten (Kimball Physics) and electroformed nickel (Buckbee-Mears), respectively. The target plate was made out of 99.95% pure tantalum (Alfa Aesar), sanded with 2400-grit silicon carbide sandpaper, degreased, cleaned, and sonicated in HPLC grade methanol. A sputtered target would have been better, but was not available.

The Dustbuster was originally designed to use 4.8 kV for ion extraction. In order to determine the possibility of operating the instrument using less power, a number of lower voltages were also tried, with all electrostatic potentials scaled proportionally. In addition, the voltage on the microchannel plate detector was independently varied from 700 to 900 volts per plate in order to determine the optimum conditions for observing the mass spectra. The signal from the microchannel plate detector was amplified with a 20x gain differentiating preamplifier (EG&G Ortec VT120) and recorded using a 150 MHz digital oscilloscope (Yokagawa 1520). Spectra were calibrated using the sodium and potassium (^{39}K) peaks. Time-equals-zero points were not directly measured, but were extrapolated using the calibration points. A total of 750 spectra were recorded.

4.7 Results of microparticle impact experiments on the Dustbuster

Figure 4.8 shows particle velocity as a function of mass for all particles studied. Measured particle velocities were generally between 1 and 10 km/s, although velocities up to 23 km/s were observed. Uncertainties in velocity and charge measurements were approximately 5%. Figure 4.9 shows the mass and charge of all detected particles. Also included are lines of constant surface charge density for ideal iron spheres in the range of the measured particles. The charge density of nearly all the particles in this experiment were at least an order of magnitude below the field desorption limit, 2×10^{10} V/m, consistent with previous results using similar charging methods [2, 3, 5]. Interestingly, the larger particles were charged to a fairly constant surface charge density (5×10^{-3} C/m^2), while particles below 2×10^{-16} kg follow more closely a curve

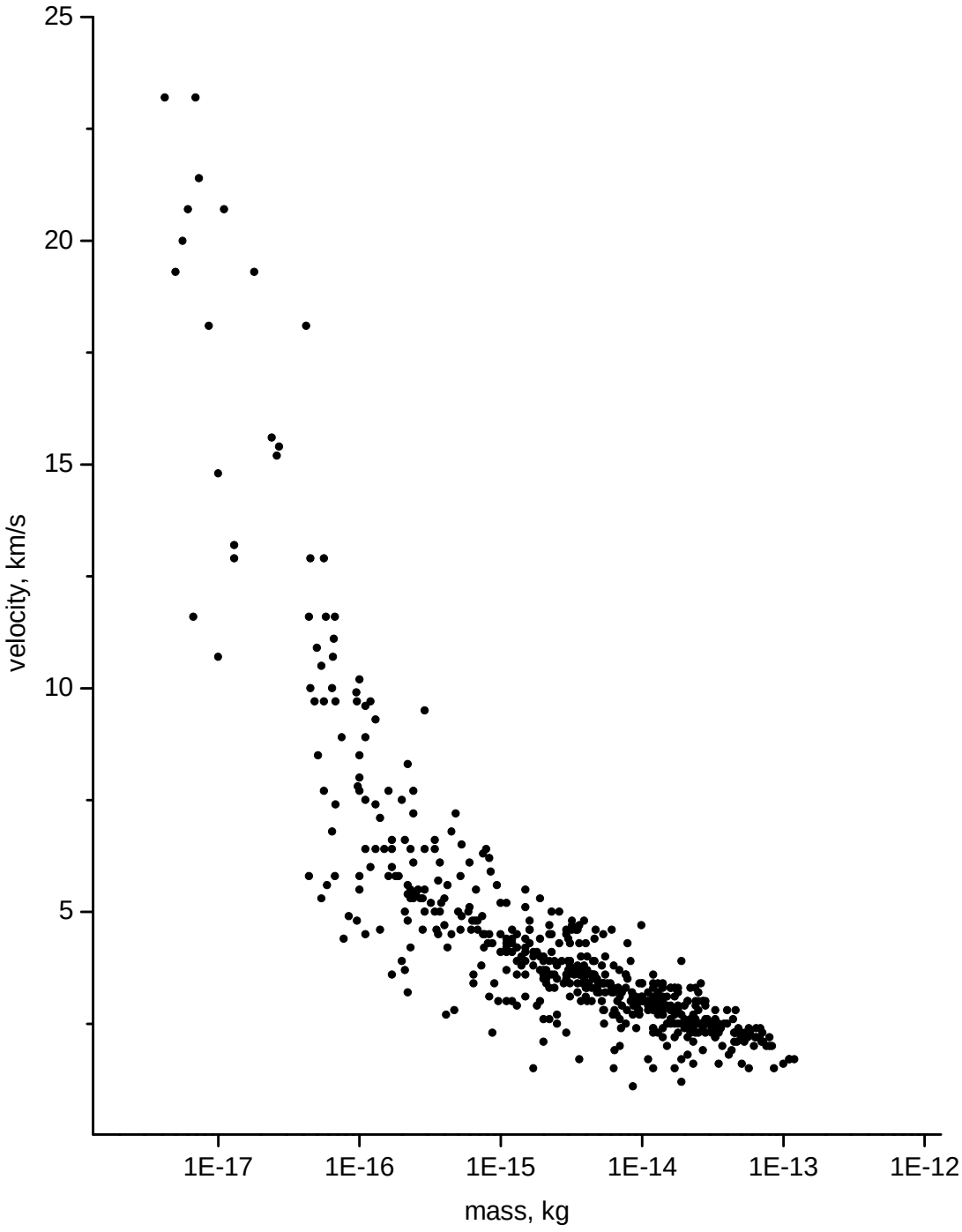

Figure 4.8. Velocity and mass of microparticles studied.

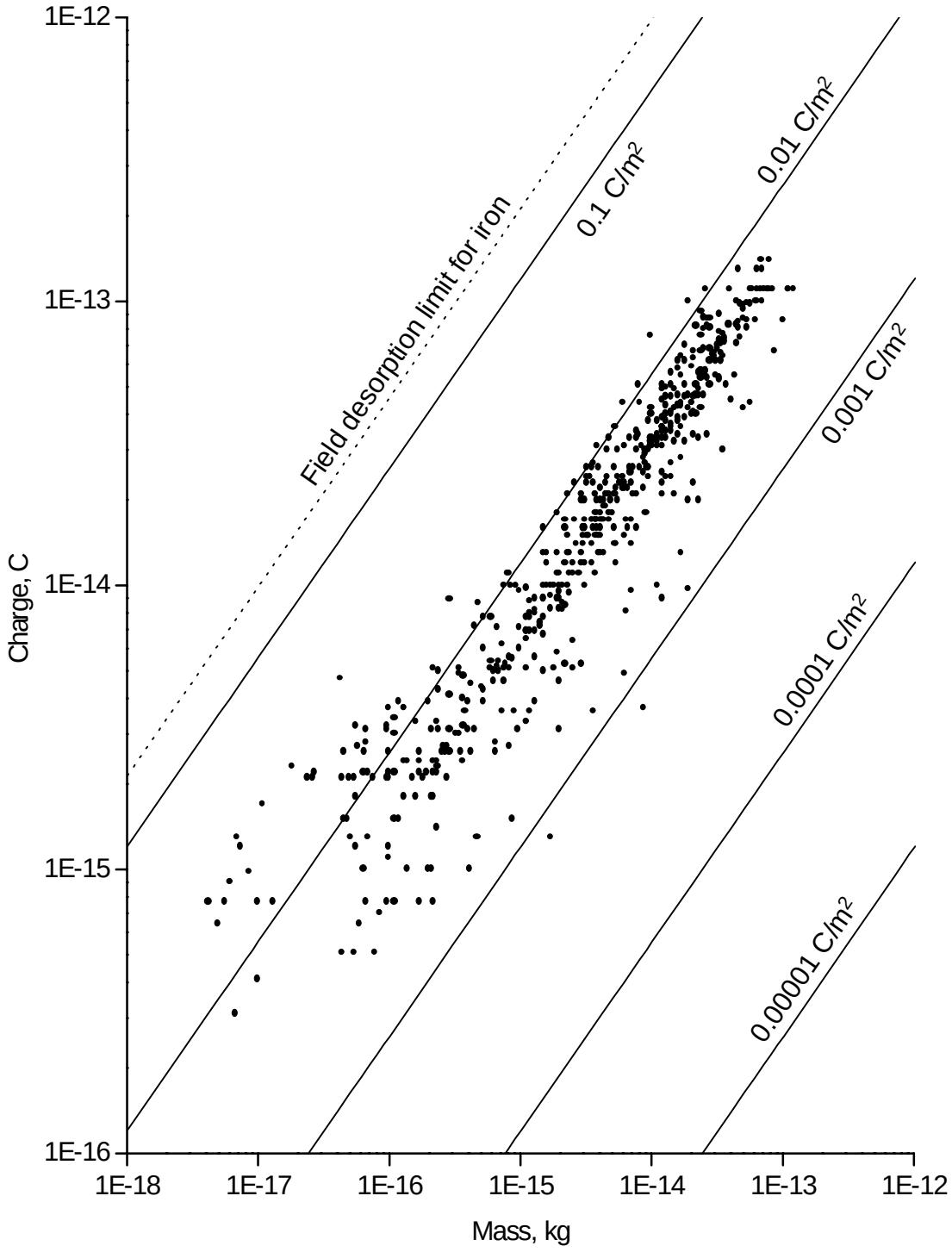

Figure 4. 9. Mass and charge of accelerated microparticles, shown with lines of constant surface charge density for iron spheres.

of constant surface potential. During the experiments, a large number of particles struck the Dustbuster and triggered the recording electronics, but had too small a charge to be detected by the cylinder electrodes in the accelerator flight tube. Nonetheless, most of these particles generated interpretable mass spectra.

Figures 4.10 and 4.11 show representative mass spectra for particles with defined and undefined velocities, respectively. Spectrum 4.10a, typical of roughly 20% of the impacts, shows only sodium (Na^+) and potassium (K^+) ion peaks with high mass resolution. Spectrum 4.10b shows a hydrogen ion (H^+) peak and unusually broad sodium and potassium peaks. Spectrum 4.10c shows broad sodium and potassium peaks along with a strong iron (Fe^+) peak. Similarly broadened peaks appeared in about 15% of the spectra, but sodium and potassium were the only species for which significant broadening occurred. In general, these peaks were broader for slower impact velocities. Impact angle, which was varied from 0º to 23º, did not have any noticeable effect on the amount of peak broadening. In many spectra, the number of ions observed from a given *m/z* exceeded the input voltage limit of the signal amplification or recording electronics, producing the peak clipping seen in spectra 4.10c and 4.10d. Spectrum 4.10d shows peaks corresponding to hydrogen, carbon (C^+), oxygen (O^+), sodium, potassium, and iron, and a peak at $m/z = 40$, which was not positively identifiable, but was assumed to be either calcium or argon. Argon was used in the production of the copper and iron powders, and may have been incorporated into the microparticles. Thus the presence of argon in the spectra would not be surprising. Spectra 4.10e and 4.10f contain similar peaks with varying intensities. Spectra 4.10e and 4.10f showed peaks of tantalum (Ta^+) and tantalum oxide (TaO^+), and these portions of the spectra are shown as inserts. None

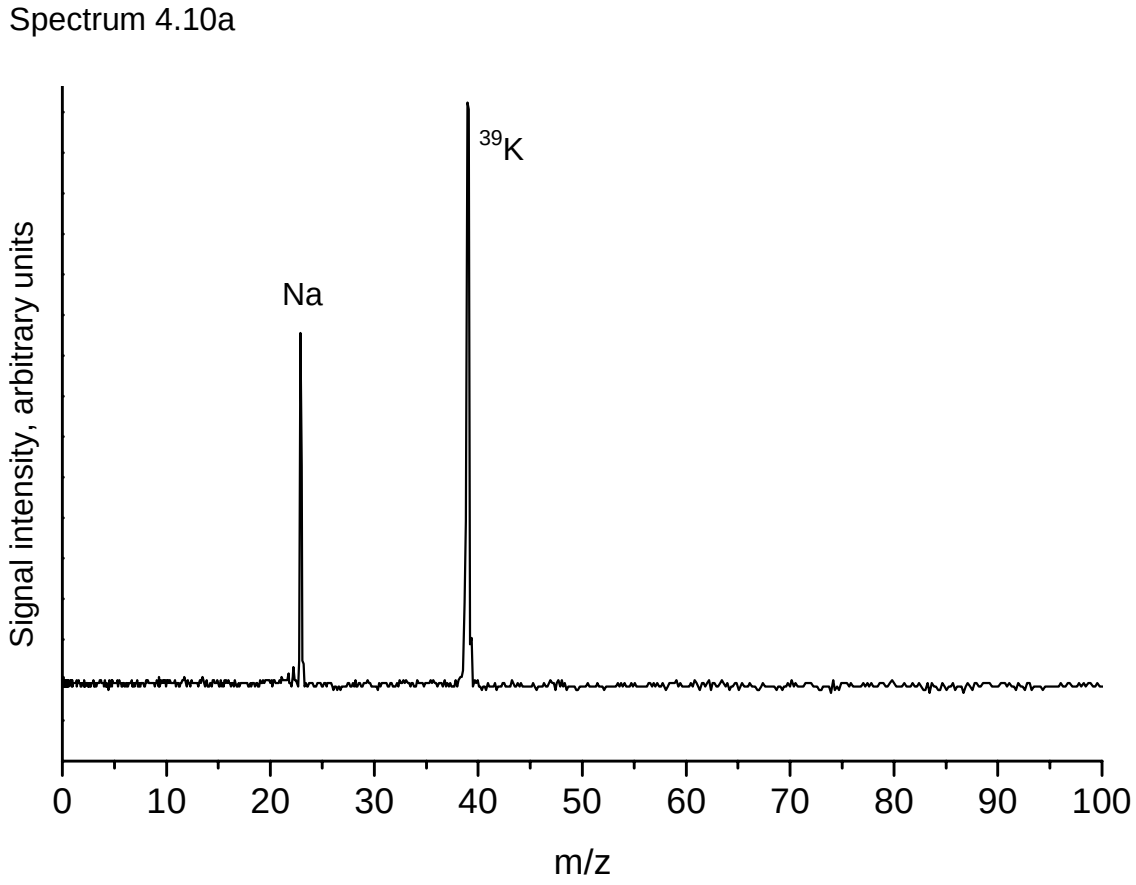

Figure 4.10. Hypervelocity microparticle impact spectra on the Dustbuster. Spectrum 4.10a was from a 1.3 μm, 2.4 km/s impact.

Spectrum 4.10b

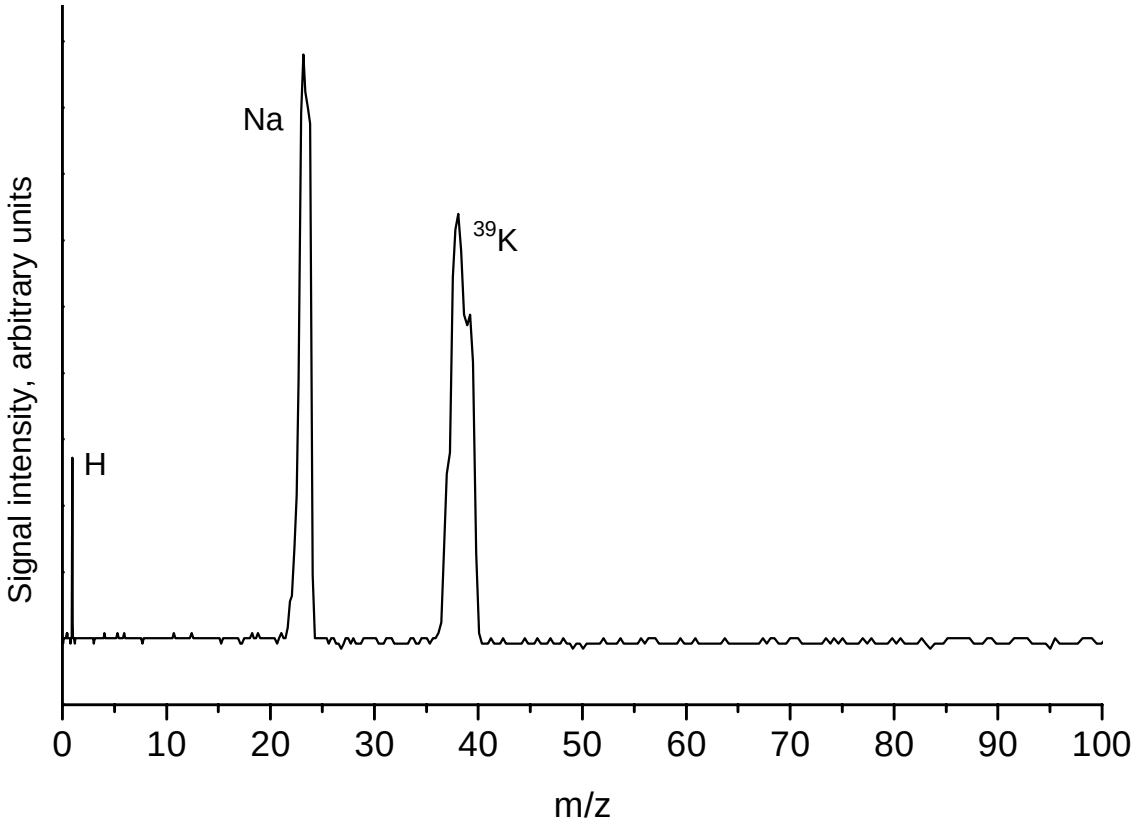

Figure 4.10. Hypervelocity microparticle impact spectra on the Dustbuster.

Spectrum 4.10b was from a 2.0 μm, 2.2 km/s impact.

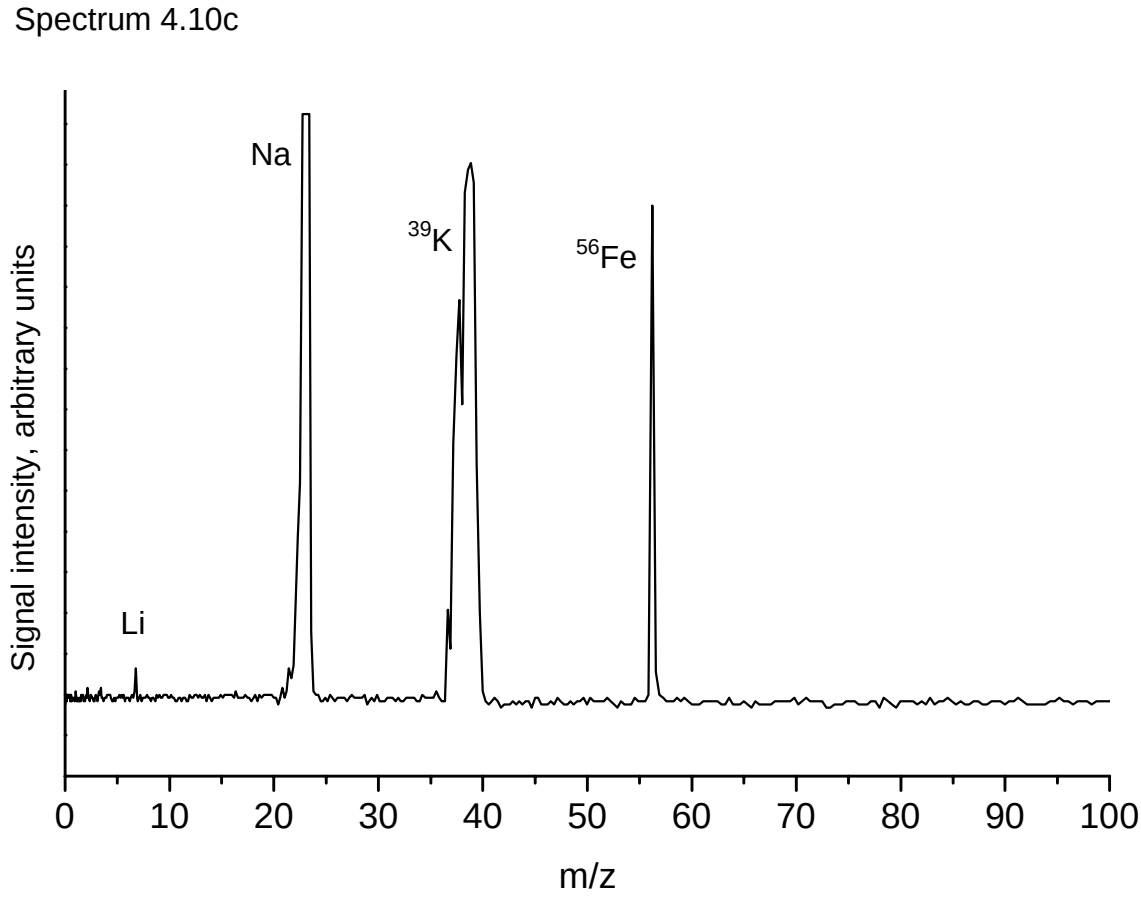

Figure 4.10, continued. Hypervelocity microparticle impact spectra. Spectrum 4.10c was from a 0.3 μm, 4.45 km/s impact.

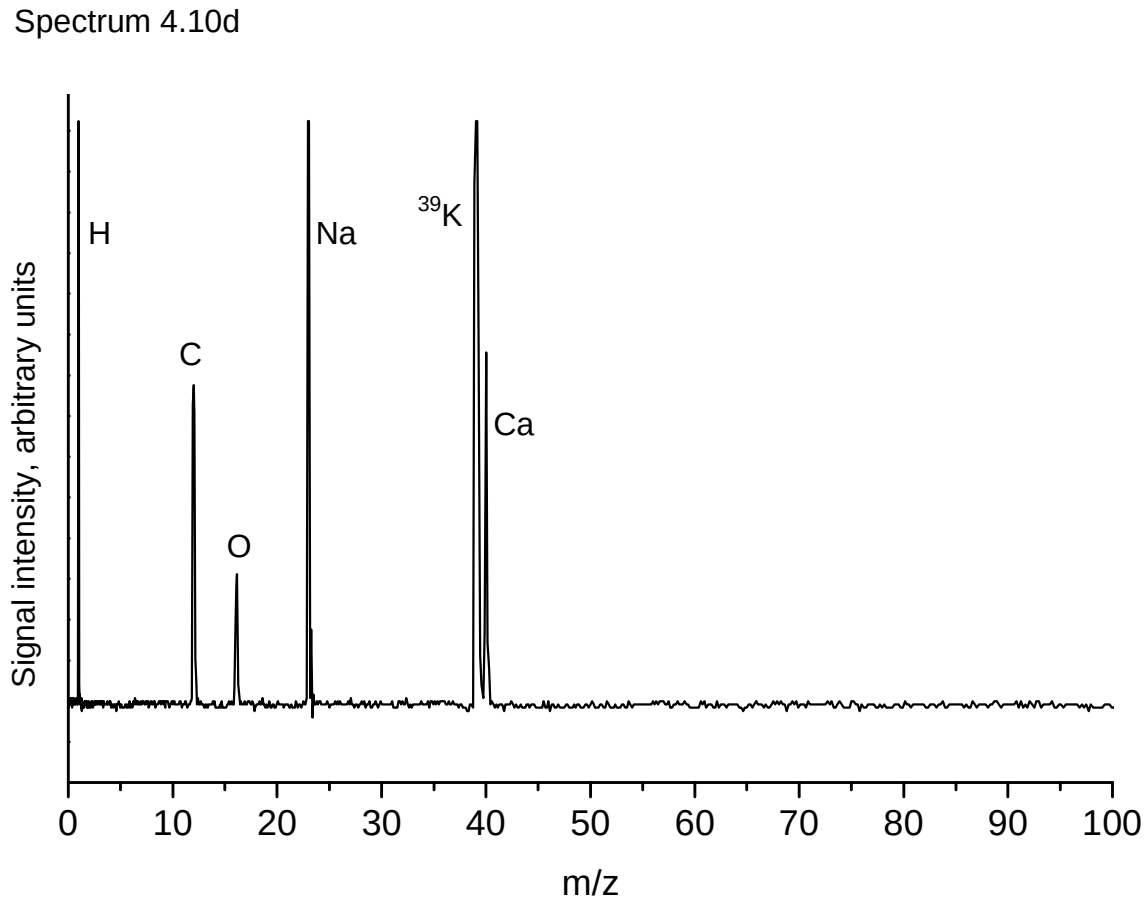

Figure 4.10, continued. Hypervelocity microparticle impact spectra. Spectrum 4.10d was from a 1.7 μm, 2.5 km/s impact.

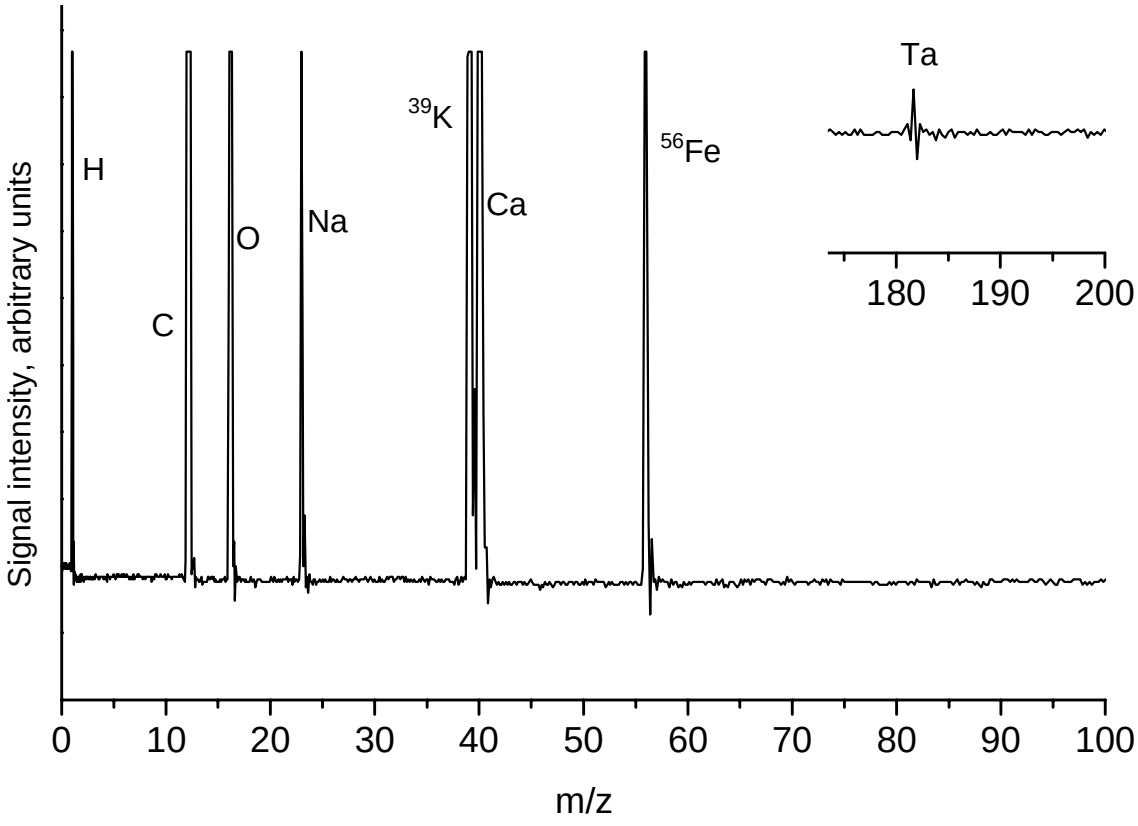

Figure 4.10, continued. Hypervelocity microparticle impact spectra. Spectrum 4.10e was from a 1.7 km/s impact.

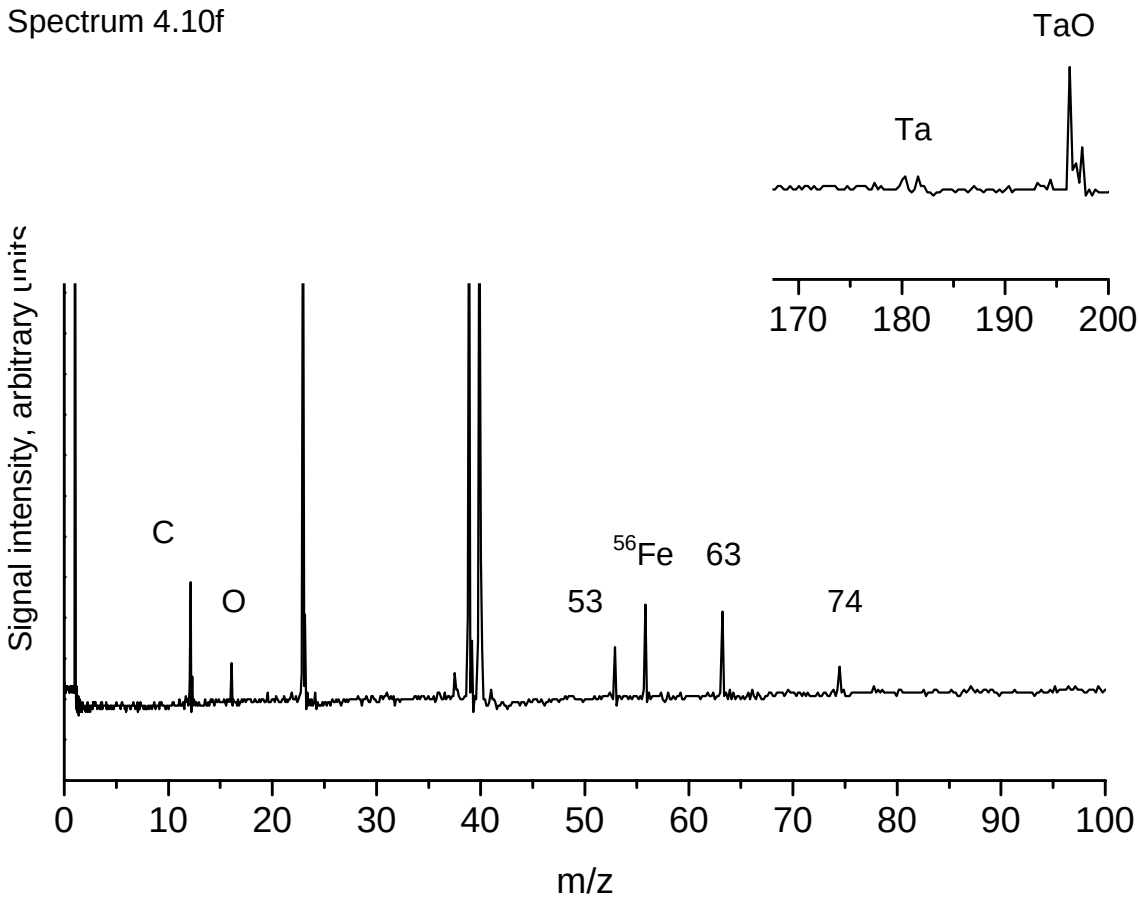

Figure 4.10, continued. Hypervelocity microparticle impact spectra. Spectrum 4.10d was from a 1.4 μm, 3.1 km/s impact.

Spectrum 4.11a

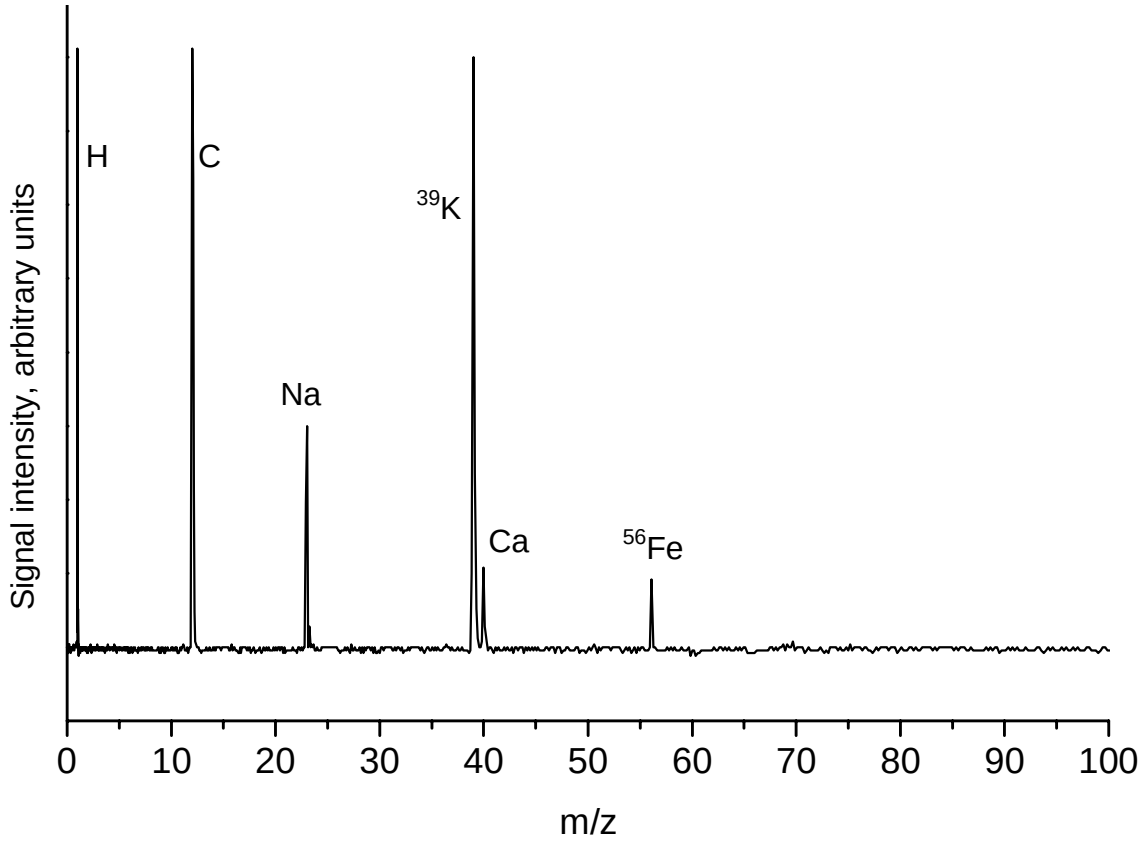

Figure 4.11. Hypervelocity microparticle impact spectra on the Dustbuster. These spectra were produced by particles whose mass and velocity could not be measured. Spectrum 4.11a is from an iron particle.

Spectrum 4.11b

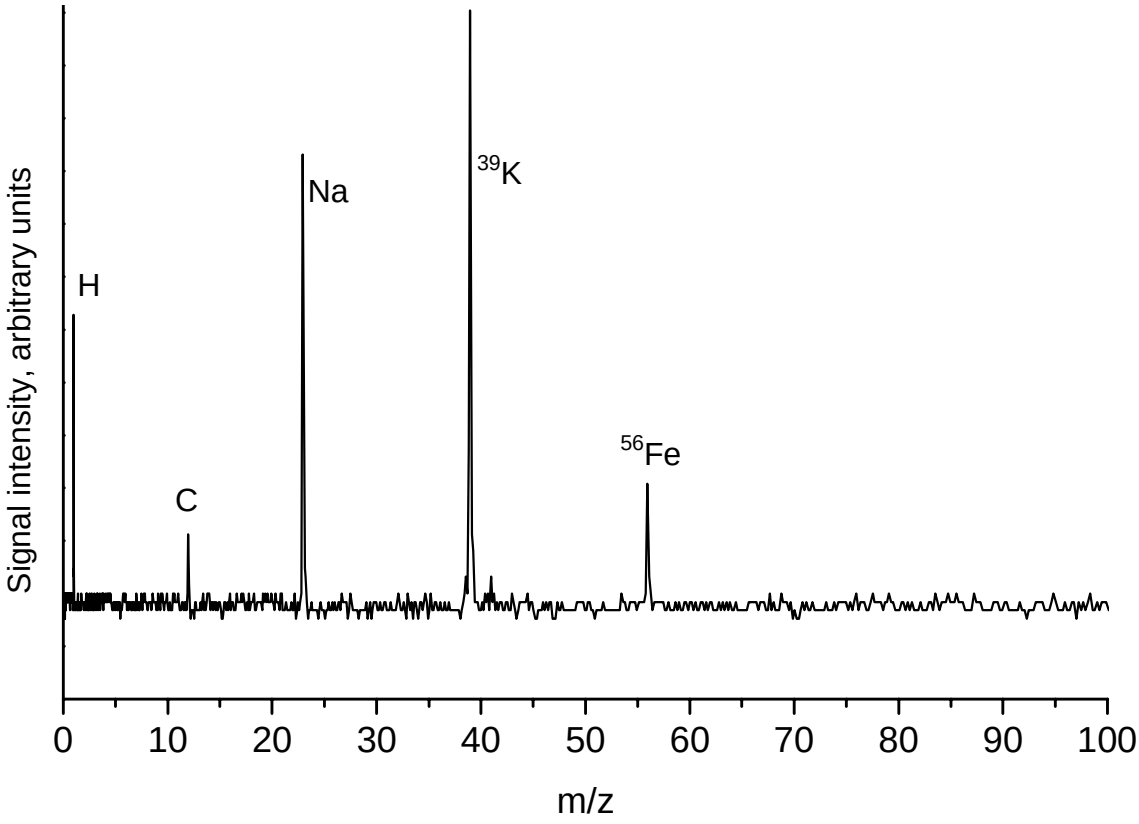

Figure 4.11, continued. Hypervelocity microparticle impact spectra on the Dustbuster. Spectra 4.11b was produced by an iron particles whose mass and velocity could not be measured.

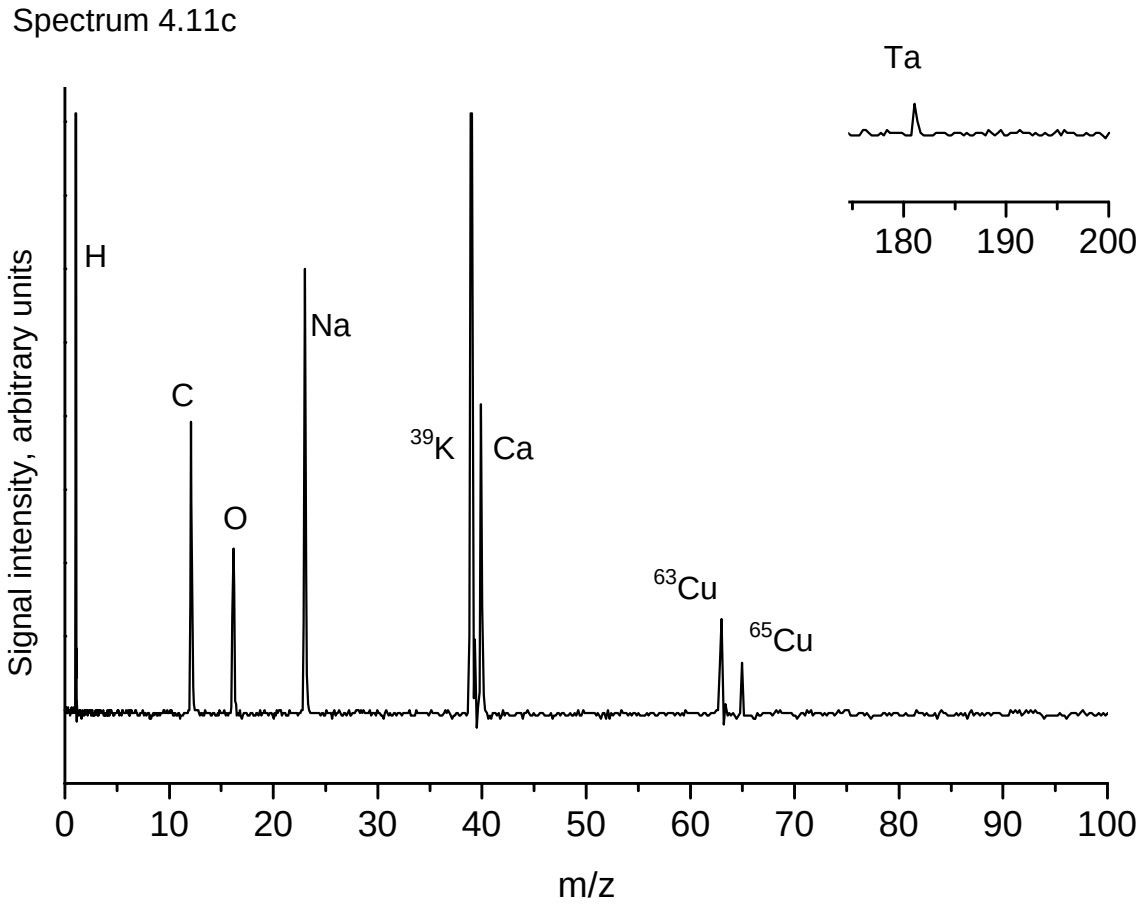

Figure 4.11, continued. Hypervelocity microparticle impact spectra on the Dustbuster. Spectrum 4.11c was a copper particle, unknown velocity or mass.

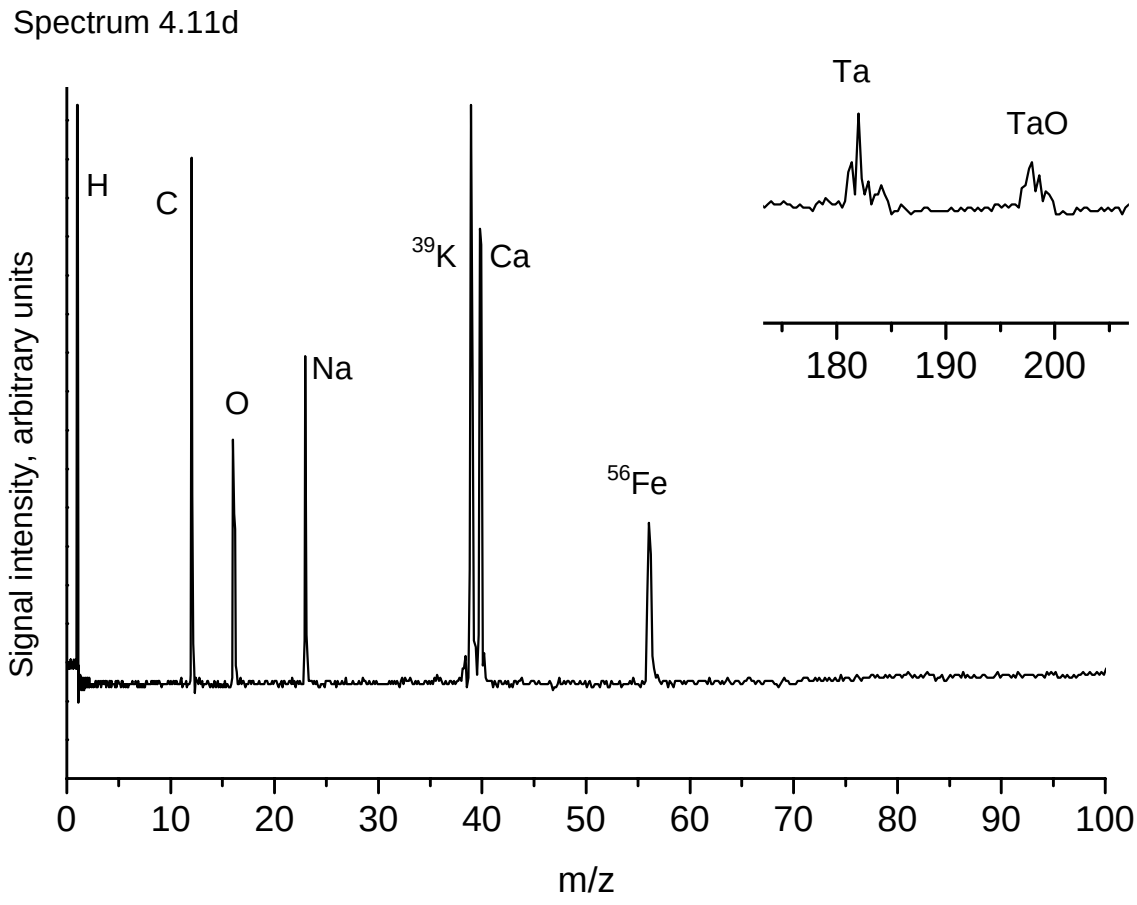

Figure 4.11, continued. Hypervelocity microparticle impact spectra on the Dustbuster. Spectrum 4.11d was an impact of an iron particle with unknown velocity or mass.

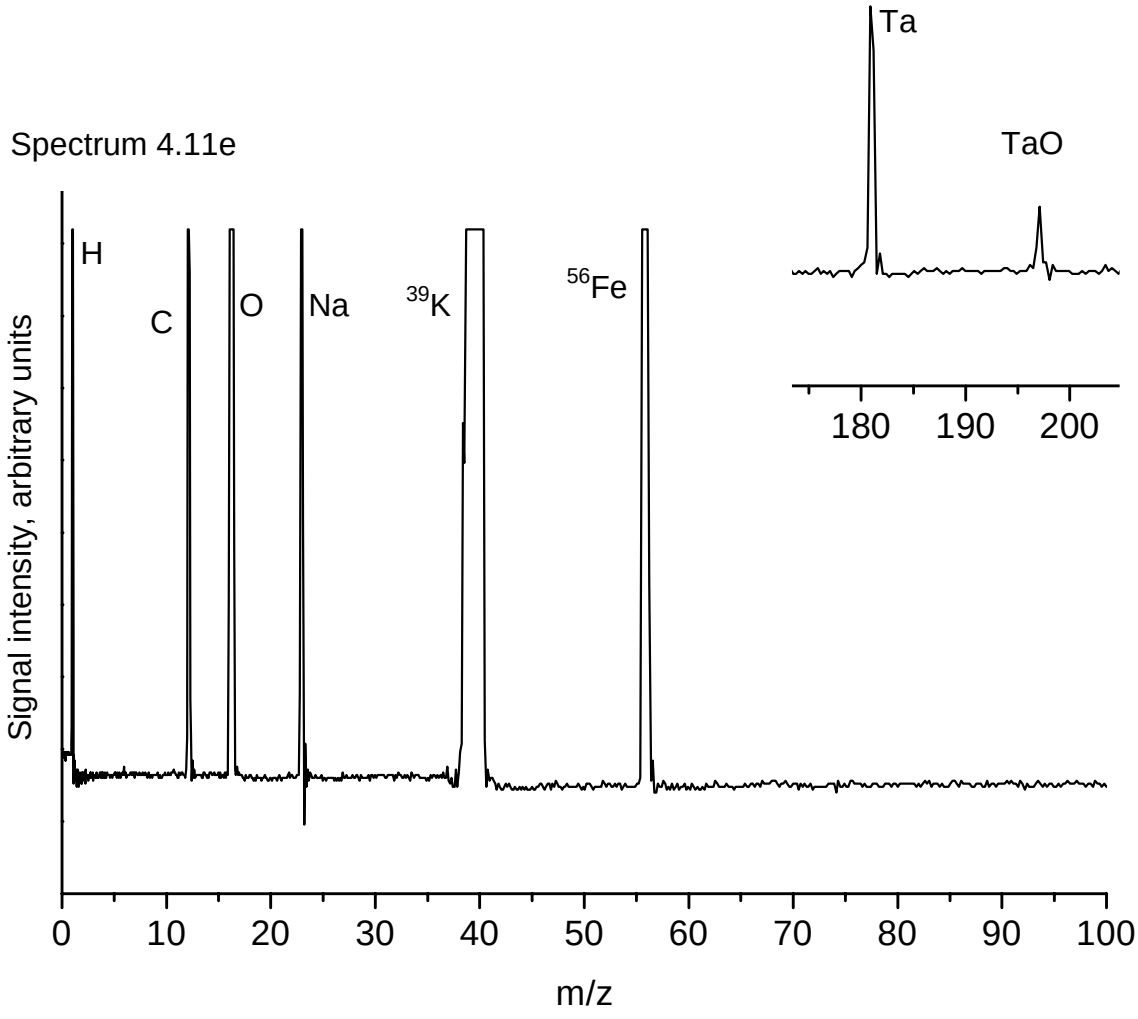

Figure 4.11, continued. Hypervelocity microparticle impact spectra on the Dustbuster from an iron particle with unknown velocity or mass.

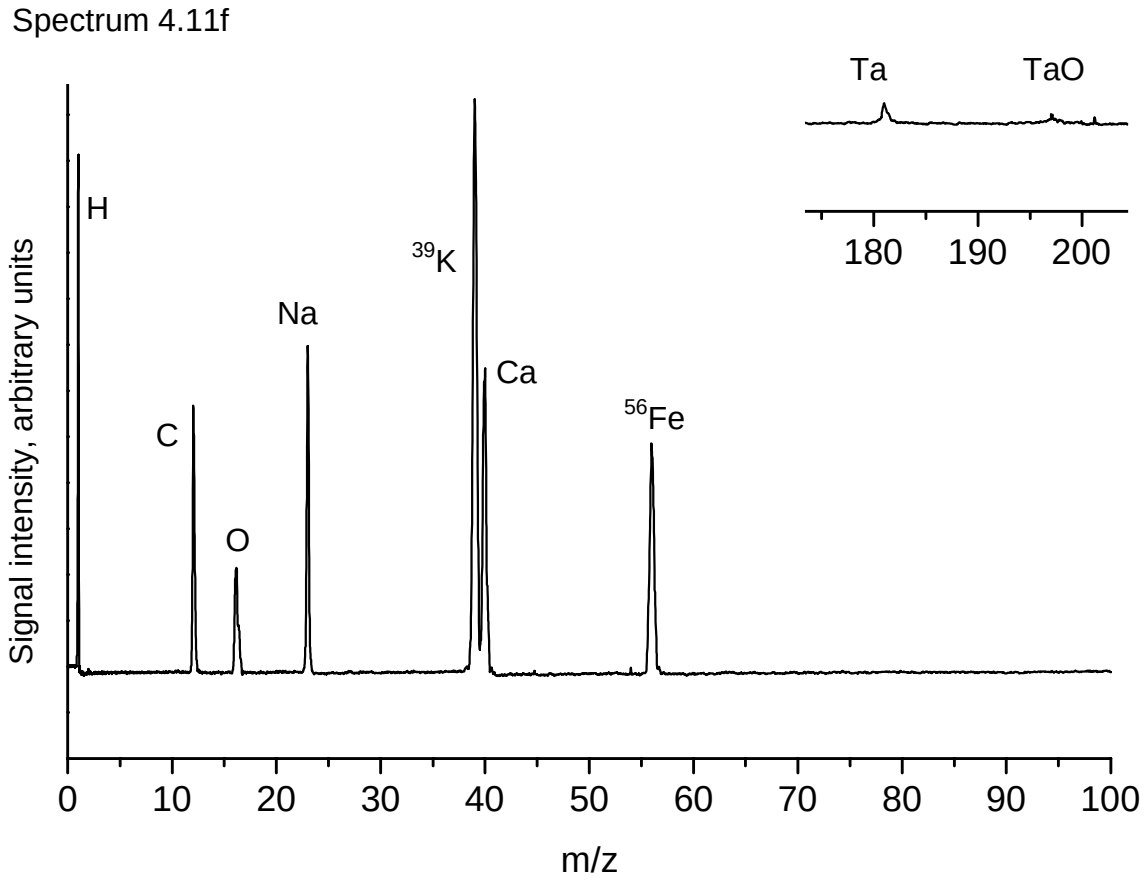

Figure 4.11, continued. Hypervelocity microparticle impact spectra on the Dustbuster from an iron particle with unknown velocity or mass.

of the spectra showed any significant peaks between m/z = 100 and tantalum. Figure 4.11 shows representative spectra produced by particles whose masses and velocities were beyond the detection limits of the cylinder electrodes. Tantalum and tantalum oxide from the target plate material are observed in some spectra. Table 4.1 enumerates all the mass peaks present in at least some of the spectra, and shows the ranges of mass resolution ($m/\Delta m$) for several species. For lighter species, particularly hydrogen, mass resolution is limited by the speed of the recording oscilloscope rather than by a distribution of ion arrival times.

In general, faster particles produced a larger number of ions, consistent with previous results [5]. As expected, neither the incident angle of impact nor the location of the impact on the target plate produced any measurable difference in the mass resolution or other features of the resulting spectra. A statistical analysis of all the spectra failed to detect any correlation between the presence or absence of any specific peaks and the velocities, masses, kinetic energies, or momenta of the impacting particles.

Several correlations exist relating the specific spectral peaks observed. For instance, tantalum (m/z = 181), tantalum oxide (m/z = 197), and a peak at m/z = 40 appear only in those spectra in which carbon and hydrogen are both present. Carbon is always present, and m/z = 40 is generally present in those spectra containing an atomic oxygen peak. H_2^+ appears only when hydrogen is present, but never when iron or copper are present. When hydrogen, carbon, and oxygen are present, their peak intensities are usually in approximately the same ratios.

m/z	% of spectra with given peak	Peak assignment	Mass resolution
1	77	H^+	20-25
2	15	H_2^+	
3	0.6	H_3^+	
7	8	Li^+	
12	59	C^+	50-150
13	0.7	CH^+	
16	28	O^+	
23	98	Na^+	5-200 (typically 100)
27	1.5	Al^+ or $C_2H_3^+$	
28	1.0	CO^+ or Si^+ ?	
39 (41)	99.5	K^+	5-200 (typically 100)
40	37*	Ar^+ , SiC^+ or Ca^+ ?	
56 (54)	16	Fe^+	150-350
63 (65)	8	Cu^+	150-350
181	9	Ta^+	300-600
197	6	TaO^+	

* Peaks may have been obscured by broad potassium lines, hence the occurrence of this peak may be more frequent than indicated.

Table 4.1. Summary of all peaks present in at least 3 impact spectra. Mass resolution ($m/\Delta m$ at FWHM) is given for important peaks.

In most spectra, peak intensities corresponding to minor isotopes, such as $^{41}K^{+}$ and $^{54}Fe^{+}$, were smaller than expected. In some spectra, minor isotopes were absent. For reference, Appendix A lists the natural abundances of all stable isotopes of elements observed in the impact experiments. These isotope anomalies were also seen in laser desorption ionization experiments both by myself (Section 3.3) and by other researchers using similar equipment [36, 37]. Several factors may be responsible for this effect. First, microchannel plate detectors are known to have nonlinear response to isotopes in some situations [38, 39]. Although MCPs have been used for careful isotope ratio measurements, corrections must be made for gain saturation and other effects [40]. In the current experiment minor isotope peaks may have been truncated or improperly sampled. Another possibility is that peaks such as m/z = 56 may have had, in addition to $^{56}Fe^{+}$, an additional contribution from a contaminant such as calcium oxide (CaO^{+}), reducing the expected intensity of other iron isotopes with respect to the principal peak at 56. If this is the case, the m/z = 40 peak may be calcium, which was not expected to be a significant contaminant in this experiment. Insufficient information exists to indicate which of these possible scenarios is responsible for the anomalous intensities of minor isotope peaks in the spectra. For a flight instrument, however, a more linear ion detector would reduce this obstacle to isotope ratio analysis.

Sodium and potassium ion peaks were observed in nearly all spectra. In many of the impacts, these were the only observed ion species. Because of their low ionization potentials (5.139 eV for sodium, 4.341 eV for potassium) and prevalence on metal surfaces, these alkali ion contaminants commonly appear in mass spectrometry involving surface ionization.

The presence or absence of certain mass peaks shows a great deal of variability between similar microparticles. This variability is sufficient to obscure correlations that might exist between measured particle parameters and spectral features. For instance, given two particles identical in mass, composition, charge, and velocity, one may produce significant C, H, and O peaks, while such peaks might be completely absent from the spectrum of the other particle. Figure 4.12 shows an example of this: three 2.6-micron iron particles (before copper dust was added to the dust source) impacting normal to the target, at 2.1 km/s, and in the same region of the target plate produce three different spectra. The origin of this variation in spectra is not clear, but illustrates the dependence of the ionization mechanism on one or more unmeasured variables. These variables may pose significant limitations on estimates of elemental composition from any cosmic dust analyzer of this type.

4.8 Charge transfer and the impact ionization mechanism

Non-metal ion peaks (H^+, C^+, O^+) have been observed in previous impact experiments, although their source is unclear. Ratcliff and Alladhadi [26] saw H^+ and C^+ peaks in their mass spectrum of a 94 km/s boron carbide particle impacting a silver-plated aluminum target. They attributed these peaks to hydrocarbon (pump oil) contamination, but no explanation was given for the lack of hydrocarbon fragment peaks. Hydrogen and carbon have relatively high ionization potentials (13.598 and 11.260 eV, respectively) and typical C-H bond strengths in hydrocarbons are 4 eV. A 9 km/s impact producing 0.4 eV per nucleon does not have sufficient kinetic energy to

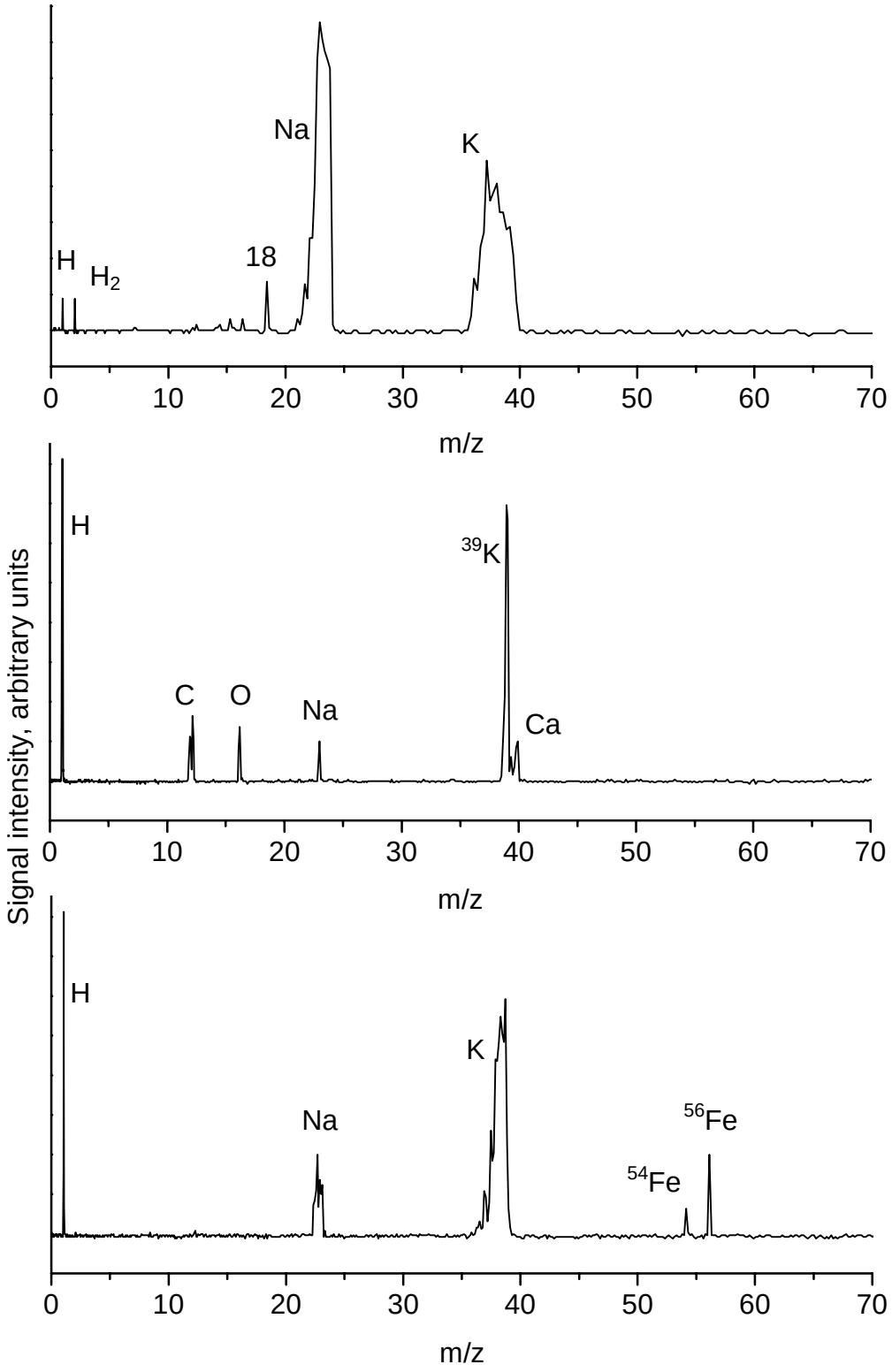

Figure 4.12. Spectra from three 2.5-μm iron particles impacting at 2.1 km/s. Despite identical impact parameters, the spectra produced are very different.

atomize and ionize species with such high bond dissociation and ionization energies [22]. Although the energy required to produce free H^+, C^+, and O^+ is much higher than the impact energy, their presence may be explained by the theory proposed by Novikov [27] and discussed by Sysoev [28, 29] and McDonnell [30]. They postulate that an electric discharge occurs between the charged particle and target surface immediately before impact. According to their model, when the charged microparticle is within approximately 1-2 μm of the surface, the high electric field causes electrons to be emitted from the target surface and strike the particle, causing electron-induced desorption and ionization. In addition, a small spot on the particle surface is strongly heated, causing thermal desorption and ionization of such species as Na and K. This model affects not only laboratory measurements with charged microparticles, but also results from dust particles in space, which are typically charged to potentials of several volts [41].

Burchell and co-workers [42] conducted an experiment in which highly charged hypervelocity microparticles passed through a thin gold-palladium foil prior to impact on a solid plate. Passage through the foil significantly reduced the particle charge, and affected velocity only minimally. Particle velocities were typically below 10 km/s. Particles with reduced charge produced fewer total ions upon impact, supporting Novikov and Sysoyev's model.

As a charged microparticle approaches an impact plate, it induces an image charge, changing the electric field in the region. Agutti [43] developed a model to estimate the capacitance between a charged particle and plate, resulting in Equation 7:

$$\frac{C}{C_0} = \ln\left(\sqrt{\frac{r}{s}}\right) + 1, \tag{7}$$

where r is the particle radius, s is the separation between the particle and the impact plate, and C and C_0 are the induced and free-space capacitance of the system. McDonnell [30] used this result to approximate the electric field, E, between particle and plate as

$$E = \frac{V_0}{s\left(\ln\left(\sqrt{\frac{r}{s}}\right) + 1\right)}, \tag{8}$$

where V_0 is the free-space surface potential on the charged microparticle. As a charged microparticle approaches the impact plate, the electric field increases until it exceeds the field desorption limit for electrons on the impact plate. At this point, electrons are emitted from the plate and strike the microparticle. Sysoev [29] estimated that electron emission begins at a distance of roughly 1-3 microns (for particles with size and charge typical of impact experiments) and continues until physical contact. Presumably, the electric field will not significantly exceed the electron-desorption limit (10^9-10^{10} V/m), although it may stay near that limit until physical contact occurs. Thus the above equations are only approximations valid within a certain range of particle-plate separation distances.

When the microparticle reaches a certain distance from the impact plate, the induced electric field will be sufficient to cancel the externally applied field. When closer than this distance, the microparticle will be accelerated toward the impact plate by the induced field. Figure 4.13 shows an estimate of the total field (using equation 8) felt by the approaching particle as a function of distance for a typical 1-micron particle with

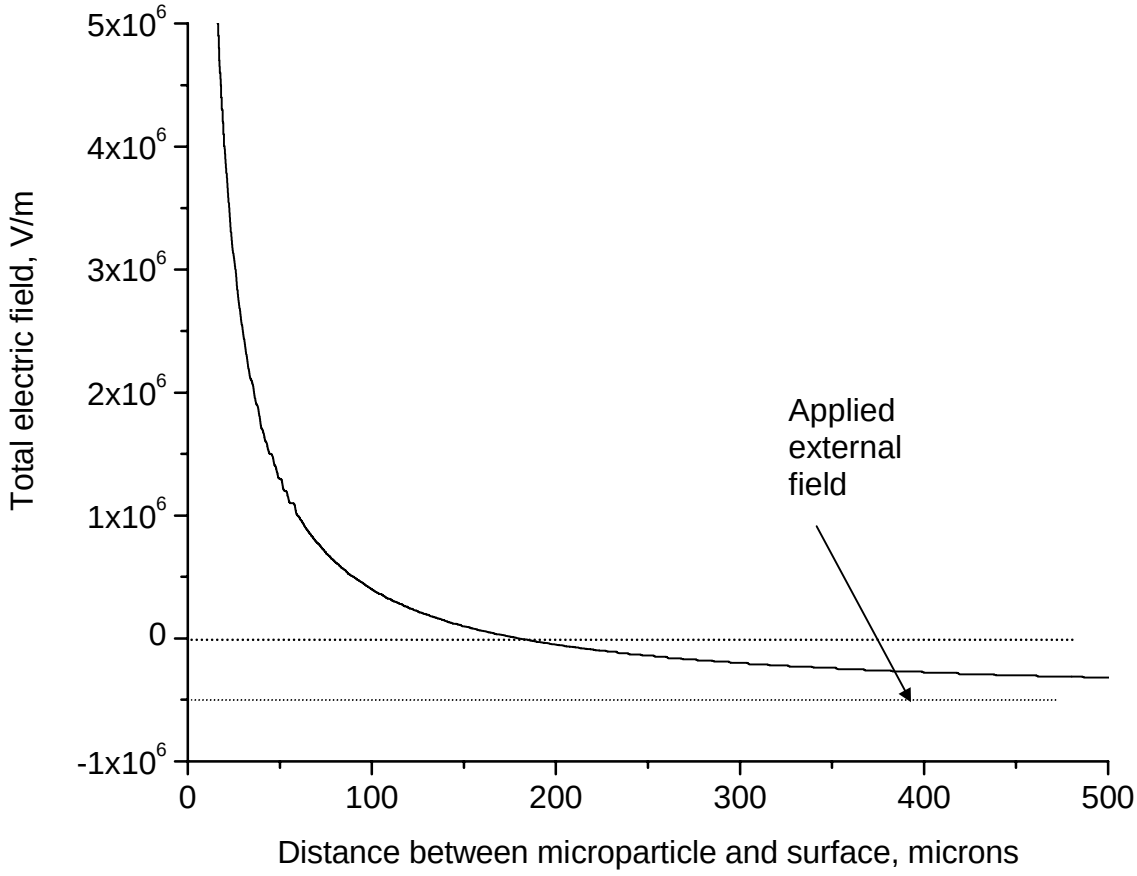

Figure 4.13. Electric field as a function of distance from target for a 1-μm, 1×10^{-14} Coulomb positively charged particle. Applied external field is 5×10^{5} V/m. Positive field is oriented toward impact plate.

1×10^{-14} C charge. At around 175 microns the field reverses direction and pulls the particle into the plate. Any impacting microparticle will thus impact the surface with a slightly higher velocity than that at which it had been traveling.

A more refined approach to this problem involves using dynamic image charge theory [44, 45]. Assuming ideal conductors, the surface charge density, σ, on the impact surface due to a point charge, q, is

$$\sigma = -\frac{1}{4\pi}\frac{\partial \Phi}{\partial z}\bigg|_{z=0} = -\frac{q}{2\pi\left(\rho^2 + d^2\right)^{3/2}}, \tag{9}$$

where Φ is the electrical potential at the surface, $\rho = 0$ is the point on the surface closest to the particle, ρ is the distance from this point along the surface, z is the distance away from the conducting surface, and d is the separation between the surface and the particle ($d = z$) [46]. Neglecting dynamic effects the acceleration on the particle due to the induced potential will be

$$a = \frac{q^2}{16\pi d^2 m \varepsilon_0}, \tag{10}$$

where m is the particle mass, and ε_0 is the permittivity of free space. As the particle nears the surface, however, the charge of the particle will be reduced by electron impact, so the acceleration function is multiplied by a decreasing function, such as an exponential decay [47]. Taking into account the electric field produced by the extraction grid (and using a superposition of solutions to the Laplace equation), the acceleration is reduced by a constant. This constant is the same as the total deceleration of the particle in the extraction region if image charge effects are ignored. Thus the particle impacts at

a velocity higher than its initial velocity, but slower than expected using simple image charge theory.

As the particle approaches the surface the electric field at the impact surface will be enhanced in some regions due to inhomogeneous surface topology. Electron emission will occur sooner than predicted using the value of the electric field calculated for an ideal, planar surface.

As electrons are accelerated toward the microparticle, they in turn induce an image charge on the particle, resulting in a greater impact energy for the electrons. The image charge on the particle is present before electron emission occurs, and increases as electrons approach the particle. To account for the finite particle size, treatment of this situation requires the full image-charge interaction potential rather than the induced dipole approximation [48], resulting in a velocity-dependent solution that can be solved numerically. The electron impact energy has been estimated for very slow electrons [49]. However, in the case of highly charged microparticles, the impact energy will be much greater. The energy with which the first electrons impact the particle surface may be on the order of 200 eV for a 1-micron particle with a charge of 10^{-14} C. In comparison, the average kinetic energy per nucleon for an impact of such a particle at 2 km/s is only 0.02 eV. For higher velocities, the impact kinetic energy increases, while the number and total energy of impacting electrons decreases. Figure 4.14 shows the relative contributions of impact kinetic energy and electron impact in ionization of iron microparticles with surface charge density of 0.005 C/m^2 accelerated to 1.5 MV. Although the magnitudes of both curves are in units of energy, the comparison is not necessarily direct. Electron impact energy affects ionization of surface species, but

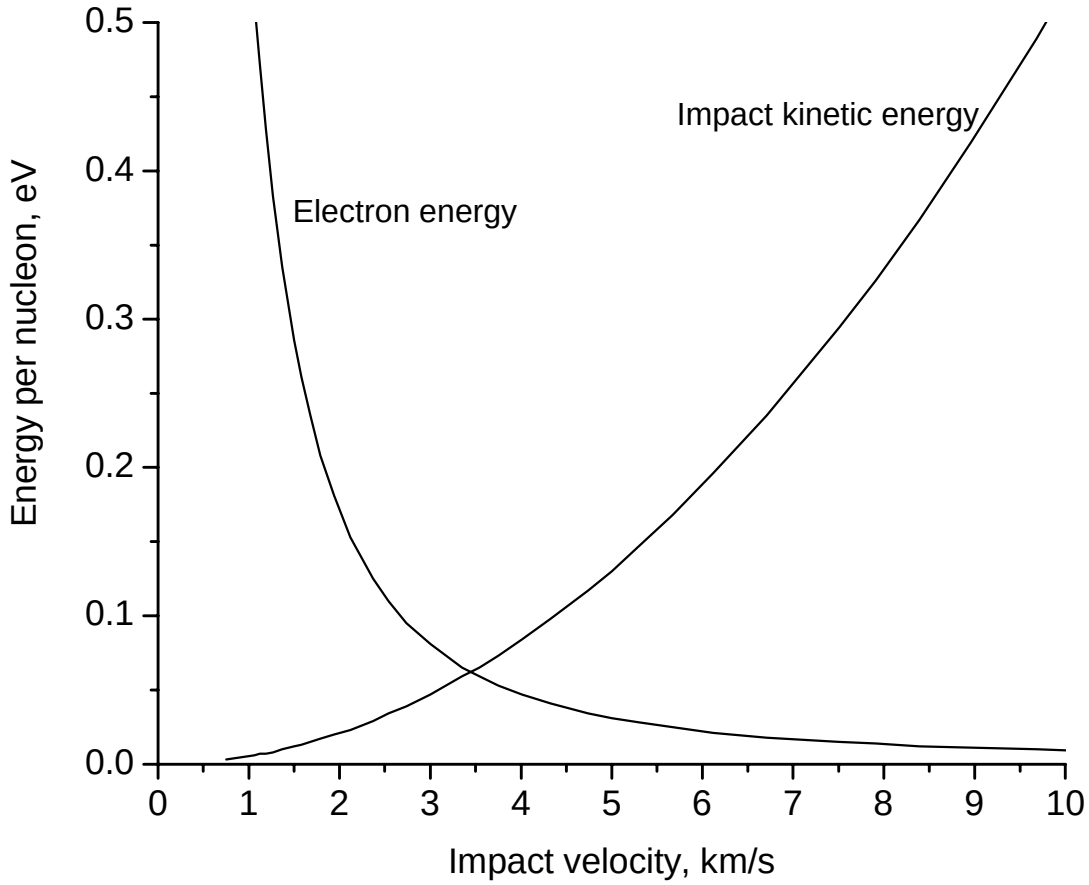

Figure 4.14. Energy dissipated in an impacting microparticle from both impact kinetic energy and from emitted electrons. The ionization efficiency, which is different for each mechanism, is not considered in this figure.

kinetic energy is proportional to the shock wave properties for the entire particle. Thus the curves in the figure show energy dissipated per nucleon. The calculations for this figure assume that electron emission begins at a separation of 3 microns for a 1-micron particle with charge of 1.5×10^{-14} C [29], and that the cube of the distance at which electron emission occurs for other particle sizes is inversely proportional to particle charge. This relation is consistent with the assumption (not used in the calculation) that electrons are emitted by the electric field where

$$E = -\frac{q}{2\pi\varepsilon_0 \left(\rho^2 + d^2\right)^{3/2}} \beta \tag{11}$$

and β is an empirical correction to account for increased electric field due to surface roughness. The calculation further assumes that electron impact energy is dissipated in the outer 10 nm of the surface [29] and that electron emission rates are exponential functions of the particle-surface separation within the emission distance. Determining which factor produces more ions at a given velocity depends on the ionization efficiency of each mechanism, which is much higher for electrons-induced ionization, but is not included in the calculation. Nevertheless, the trends in the figure are useful to illustrate the relative effects of these two ionization mechanisms in different velocity regimes. Note also that this model entirely ignores ionization of the impact plate material, which in some cases can be substantial.

The electron emission model accounts for the high energies needed to atomize and vaporize surface molecules. However, the increase of H, C, and O ions as a function of impact velocity is not explained (at least not with the simplifications used here), and may lie in the details of the electron emission rates, screening, or the impact

of positive ions on the impact surface before the particle impacts. It is interesting to note that H, C, and O ions appear frequently in spark source mass spectrometry.

Figure 4.15 shows the effect of the local electric field caused by the charged particle approaching the impact plate. Note that the ions formed prior to impact are not extracted with the uniform applied electric field, but are subject to the distortions of the induced local field. In fact, positive ions formed on the surface of the microparticle will likely be accelerated back onto the impact plate, creating more ions in a SIMS-like mechanism. These ions, in turn, are also extracted with a non-uniform field, and their fate is an uncertain one. Thus the ionization mechanism and ion trajectories associated with an impact are quite complex.

The foregoing treatment demonstrates that impact ionization is, at lower velocities, largely a surface phenomenon. In the Dustbuster experiments, accelerated particles likely had a surface coating of pump oil, which in this case consisted of tetramethyltetraphenyltrisiloxane. The O^+ peak observed could be caused by oxygen from the pump oil, by metal oxides on the particle surface, or by adsorbed gases, dissociated and ionized by field-emitted electrons prior to impact.

If ionization is enhanced at a particle surface, the quantity and type of ions formed in any given impact will not be representative of the particle composition as a whole. Impact ionization models, such as hydrocode simulations, that neglect electron-induced ionization mechanisms may lead to incorrect interpretations of real impacts involving charged particles [22]. Previous results from comet Halley [15, 16, 19], which showed an excess of H, C, N, and O in the impact mass spectra, may have seen a surface enrichment of these elements caused by sublimation of more volatile surface

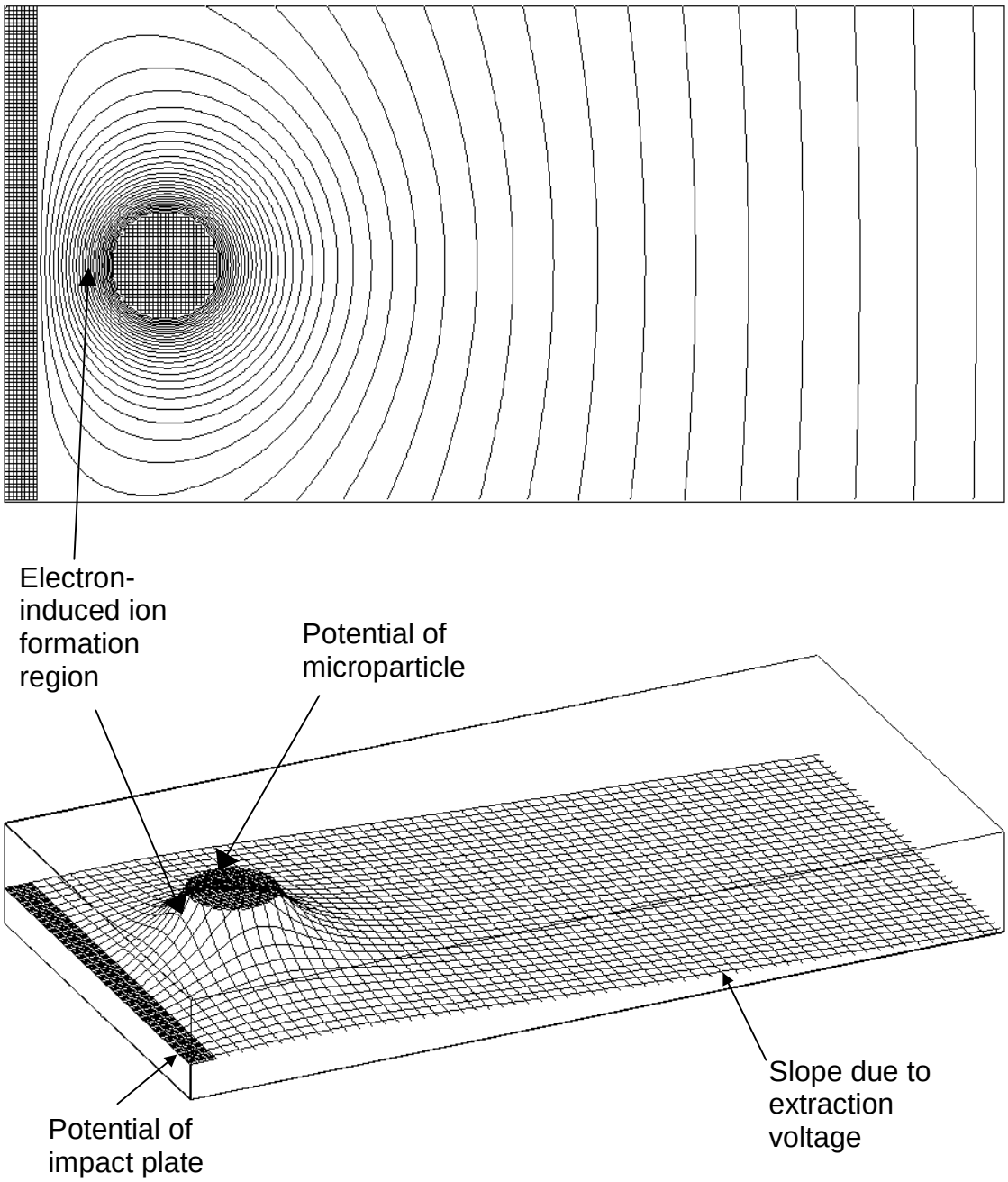

Figure 4.15. Electrostatic potential contours (above) and potential energy surface (below) for highly charged microparticle approaching a planar conducting surface. Note the nature of the potential energy surface at the point at which ions are formed during electron-induced ionization. Ions in this region are accelerated back to the impact plate.

components. The concentration of organics on the particle surfaces may or may not have been representative of the bulk cometary composition.

Both in the Dustbuster and other instruments, electron-induced ionization may also occur as particles pass through grids and come close to a grid wire. For instance, in the Dustbuster, 15% of 1-μm particles pass within 2 μm of a grid wire before they reach the impact target. Inconsistent electrical interactions may produce different mass spectra for otherwise identical particles. Similarly, field emission of electrons from the target plate will vary with the microscale topology of the impact surface. This topology may affect the quantity and nature of ions produced in an impact. Both of these effects have implications for *in situ* flight instruments. Impact cratering of a target plate, which can be extensive in some dust environments, would change the ionizing characteristics of a target plate over time. Also, particle charge measurements are necessary in order to predict the specific ionization mechanism responsible for a given spectrum.

A few other unusual observations deserve comment about the Dustbuster results. As seen in Figures 4.10 and 4.11, some spectra exhibit unusually broad Na^+ and K^+ peaks, although other ion species seem unaffected. Because the Dustbuster uses a reflectron, it is unlikely that these broad peaks are caused by differences in the initial kinetic energies of the ions. More likely, these ions are produced over a longer time scale than the other ions. For broadened peaks from slower impacts (1.5-2.5 km/s), the peak widths correspond to roughly 300 ns, while faster impacts produce less broadening. It is possible that these broad peaks arise from particles that were heated by electron bombardment while passing through the acceleration grid. Such particles would emit sodium and potassium ions all the way through the acceleration region. Computer

simulations of this situation using SIMION ion trajectory software [50] show that only those ions emitted within 300-400 μm of the target plate would have the correct energy and trajectory to reach the ion detector. The combination of being formed early and gaining less kinetic energy would result in an arrival time of about 0-300 ns earlier for these ions, consistent with observations. Of course, this demonstrates only the possibility that peak broadening is caused by thermal emission. The alkali ions might be broadened due to plasma screening, long-duration thermal ionization, or some other unusual effect. In some spectra the potassium peak may be overlapped with calcium, also producing a single, broad peak.

Charge-induced ionization may occur in one other situation of note. As microparticles in a van de Graaff accelerator are charged by the charging needle, a similar charge interaction occurs. In this case, of course, the particle is moving more slowly, and the electrons are moving from the particle to the charging needle (the opposite of the situation during an impact). Shelton [2] reported that the limiting factor in microparticle charging was not the theoretical maximum charge the particle could support. Rather, the charging was limited by the destruction of the charging needle at high voltages. If the charging needle were at a voltage higher than roughly 45 kV, the needle material would be ablated during the charging process. This is the same electron-emission ablation (and possibly ionization) that occurs during impacts. The possible effects of charging on the microparticle have not been explored. An experiment to observe ions formed during this process would be useful to further study the impact ionization process. Another useful experiment would involve deceleration of a charged microparticle immediately prior to impact. This can be accomplished by holding the

impact plate at the same potential (or nearly the same) as the potential at which microparticles are formed. In this case the impact would have insufficient kinetic energy to produce ions, so any ions formed would presumably be the result of the electrical interaction.

As electrons strike the charged microparticle, low-energy bremsstrahlung radiation should be emitted, although this has not been verified experimentally. A treatment on theoretical bremsstrahlung cross sections for electrons striking negatively charged microparticles is given by Jung [51].

4.9 Simulating cometary dust: ice particle impact experiment

Laboratory experiments on accelerated microparticles have been limited to conducting substances. Although most of this work used metal particles, a few experiments reported using metal-coated latex microspheres. However, an important component of cometary debris consists of particles composed largely of ice. Microparticle ice impacts have received little attention.

A similar phenomenon, cluster impact, has been studied in detail. Impacts of neutral water clusters produce charged cluster fragments or free ions based on impact speeds [52]. Positively charged [53] and negatively charged [54] water clusters show similar effects. Water cluster impacts typically involve aggregates with up to around 5000 molecules, corresponding to a particle size of 7 nm. Impacts of larger clusters, usually referred to as massive cluster impact, have been used to produce secondary ions for mass spectrometry [55, 56]. In this case, however, the clusters consisted of glycerol,

and were produced using an electrohydrodynamic gun (similar to electrospray). In fact, a glycerol particle source for massive cluster impact is available commercially from Phrasor Scientific (Azusa, CA). Glycerol or mixtures with glycerol are used because they neither freeze nor boil as they are exposed to vacuum. Williams and Aksyonov [57] have modified this source and produced massive clusters composed of aqueous ammonium acetate. They then accelerated these charged clusters through 8 kV and impacted them on surfaces. Dissolved biomolecules were efficiently ionized, and ammonium acetate complex ions were also observed in large abundance. High concentrations (2 M) of ammonium acetate were required to produce these results. Unfortunately, their experiment included no method to measure the impact velocity of the massive clusters.

We became interested in ice particle impacts when the Dustbuster was being considered for inclusion on the Deep Impact mission. The Deep Impact spacecraft will intercept comet Tempel 1 in July 2005. The Deep Impact spacecraft will "launch" a 370 kg impactor that will collide with the comet at a velocity of 10.2 km/s. The impact will produce a considerable amount of debris, which will be observed by video equipment on the spacecraft. We therefore began a research program aimed at understanding hypervelocity impacts of ice. These studies involved producing highly charged ice particles in vacuum, accelerating them onto the Dustbuster or other mass spectrometer, and observing the ions produced.

Several difficulties were encountered in these efforts. First was the difficulty of introducing water particles into vacuum. Second was finding a way to apply a sufficiently high accelerating voltage without suffering glow discharge problems.

Attempts to introduce electrosprayed microdroplets into vacuum through differential pumping were unsuccessful, probably because of skimmer alignment issues. Attempts to electrospray directly into vacuum were also unsuccessful due to freezing/boiling at the spray tip, and also because of glow discharge from the accelerating voltage. The use of a smaller electrospray tip and different spraying solution might have overcome this obstacle, but this course was not pursued.

Small, charged liquid droplets can be produced using a vibrating orifice aerosol generator (VOAG) [58]. The operational principal of a VOAG is illustrated in Figure 4.16. Water or another liquid is forced through a small orifice, producing a cylinder (jet) of liquid. Because the surface area of a cylinder is greater than the combined surface areas of several spheres with the same volume, the liquid jet is unstable, and tends to break up into droplets. The breakup of liquid jets was observed experimentally as early as 1833 [59], and was the subject of various works by Rayleigh [60, 61]. Rayleigh derived the natural breakup wavelength for a jet of water with diameter, D, as

$$\lambda = 4.508D. \tag{12}$$

In a VOAG, a piezoelectric element superimposes small pressure waves on the jet of liquid corresponding approximately to the natural breakup frequency. The jet of water then breaks up into highly monodisperse droplets. Figure 4.17 shows an example of monodisperse droplets produced using a 15-μm orifice with a piezoelectric frequency of 52 kHz. In this figure, droplets are observed by their disruption of a highly focused HeNe laser beam through which they pass. The laser beam intensity is measured using a fast photodiode, and the resulting signal shows the frequency of droplets formed. Droplet size is determined using the known flow rate and particle frequency.

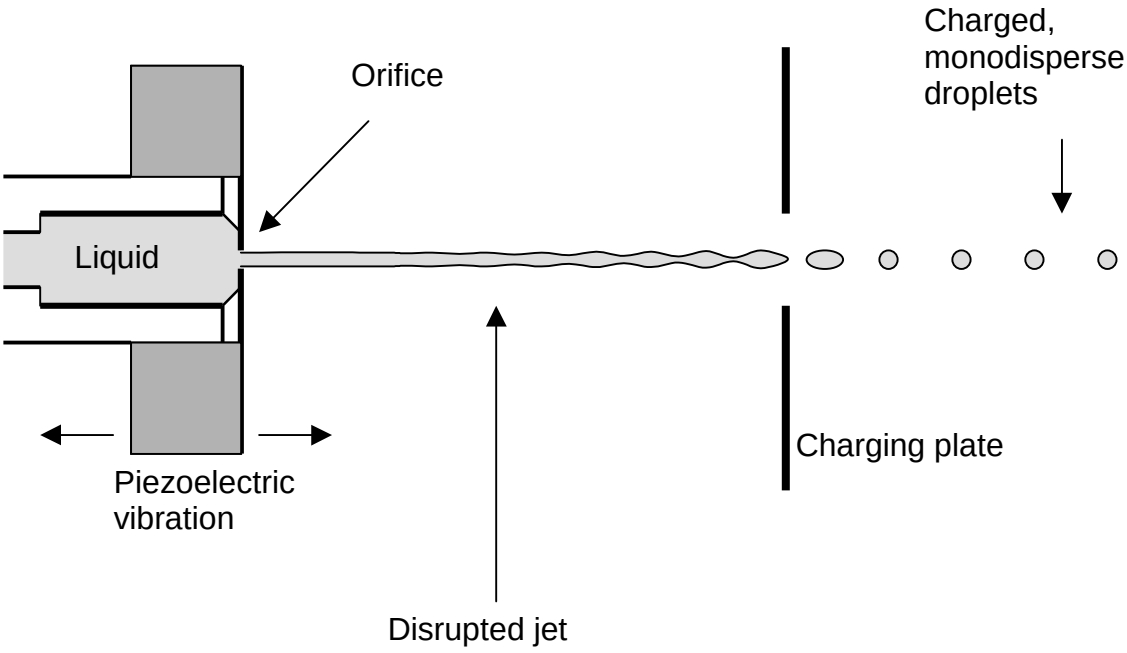

Figure 4.16. A vibrating orifice aerosol generator can be used to produce monodisperse, highly charged water droplets, either at atmospheric pressure or in vacuum.

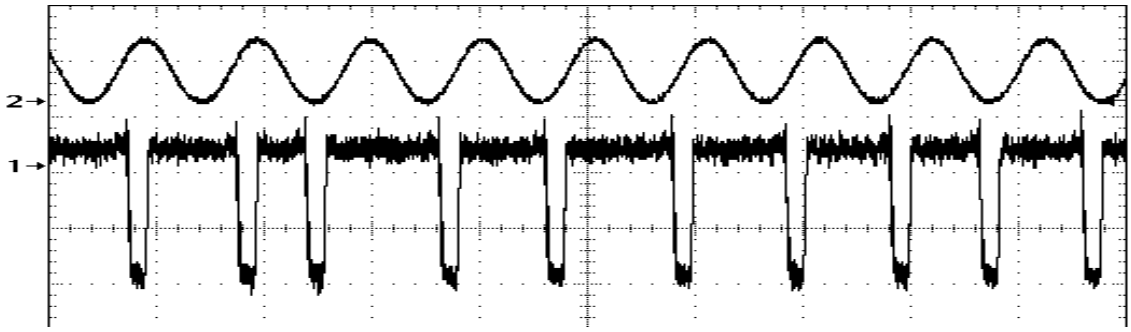

Figure 4.17. Droplets produced using a vibrating orifice aerosol generator are monitored by their obstruction (defocusing) of a HeNe laser beam. Top trace is the peizoelectric driving frequency, 52 kHz. Bottom trace is the signal on a photodiode placed in line with the laser beam. Droplets are produced using a 15-μm orifice, resulting in a particle size of 28 μm.

Droplets formed using a VOAG can be charged simply by placing an electrode in front of the orifice. Due to mechanical constraints, the orifice must be supported on the outside by a metal plate, so the electric field immediately at the orifice is very small. However, the jet of water remains intact for a few mm. The electric field at the end of the continuous jet is the important factor in the charging of the droplets. The charging plate must be placed after the point at which the jet of water breaks up into droplets so that droplet formation takes place within the high electric field.

The vibrating orifice aerosol generator has two main advantages over electrospray for producing highly charged water/ice droplets in vacuum. First of all, the liquid remains in a relatively large body, and is in contact with metal up until the point at which it enters vacuum, allowing better thermal contact with the liquid as compared with a thin column of liquid in an thermally insulating (silica) electrospray tip. The liquid is less likely to freeze before leaving the orifice. Of course, the column of water takes some time to break up, during which time the liquid could freeze and prevent droplet formation. On the other hand, the liquid is moving quickly in a VOAG (typically 5-10 m/s). The second advantage is that the liquid undergoes a sharp pressure gradient at the orifice, so boiling is less of a problem than in electrospray, where the hydrostatic pressure drops gradually near the tip and bubbles often disrupt the spray [57]. One disadvantage of a VOAG is the size range of particles possible. Droplet sizes are generally 1.5 to 3 times the size of the orifice, depending on the flow rate. Orifices are available down to 1 micron, but become more difficult to use with small sizes. In addition, a narrower liquid jet will freeze faster than a thicker jet. Droplet sizes are thus limited to a few microns.

Preliminary experiments have successfully produced 25-μm charged droplets, although no attempts to accelerate the particles have been made at this point.

4.10 Energy analyzer as a high-flux dust mass spectrometer

Despite the marginal success of the energy analyzer (Sections 4.4 and 4.5), it may have an appropriate application in another area. The PIA, PUMA, and CIDA cosmic dust mass spectrometers were designed for environments with high concentrations of dust, such as the vicinity of a comet [15, 62]. However, the large size and mass of these instruments makes them less compatible with NASA's current objectives of smaller, cheaper spacecraft. Smaller time-of-flight mass spectrometers, however, run into limitations of mass resolution. First of all, shortening the instrument can increase deviations from the paraxial approximation. Thus focused ions have greater spherical aberration. Factors related to spherical aberration, such as astigmatism and grid scatter, are also affected. The difference in flight times between ions of different mass is smaller, so focusing must be better to maintain sufficient resolution. Space-charge effects become more important, both because of the need to have narrower arrival time distributions, and also because the physical dimensions of the instrument (and ion beams) are reduced. A smaller instrument requires both faster ion detector response and faster signal amplification and recording, although these are less of an issue thanks to continuing advances in detector technology.

The energy analyzer design overcomes these limitations. Modifications to a flight instrument design might include features shown in Figure 4.18. The instrument

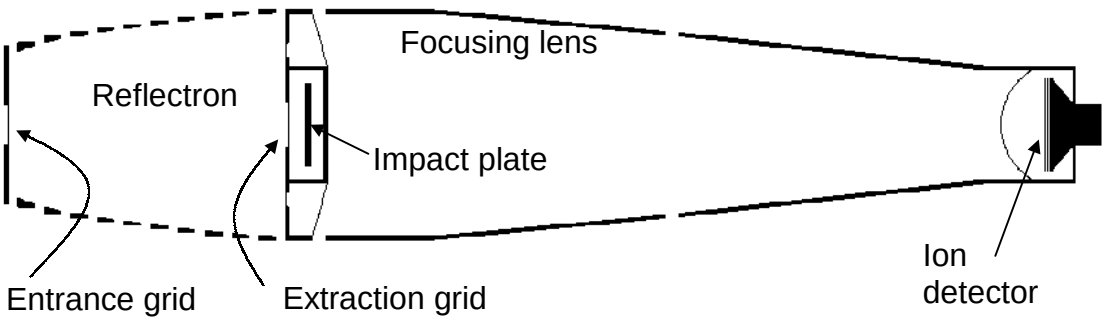

Figure 4.18. Time-of-flight mass spectrometer for high-flux cosmic dust analysis.

has a small (1 cm^2) effective impact area, so it is suitable for dust analysis in regions of the solar system with high concentrations of dust. The set of rings forms an aperture that effectively reduces the spherical aberration of the ion beam to whatever extent is needed to obtain the desired mass resolution. Of course, the narrower the window of admitted ions, the lower the instrument sensitivity. However, dust impacts typically produce a sufficiently large number of ions that even a tenfold reduction in ion transmission will still yield strong signal [5, 7, 10, 63]. By allowing a ring of ions to traverse the drift tube, space-charge effects are much less than they would be if the ions were focused into a narrower beam.

An additional feature of this instrument design is that the ion detector is completely protected from stray particles and radiation that might otherwise cause damage.

One problem encountered by the PIA and PUMA instruments is that of target cratering. The more micro-craters are produced by impacts, the less homogeneous becomes the ion extraction field. This inhomogeneity produces essentially the same effect as grid scatter: the ion beam spreads out laterally. PIA and PUMA remedied this problem by using a scrolling impact plate: a fresh impact surface would replace a plate that had become too cratered for proper ion focusing. The proposed instrument solves this problem another way: the ring aperture filters out any lateral spread, whether from the distribution of initial kinetic energies, grid scatter, or inhomogeneities in the extracting field. Thus the impact plate can become extensively cratered without affecting instrument performance.

The modified energy analyzer design has been evaluated using SIMION 7.0 ion trajectory software [50]. For simulations the instrument dimensions were as follows: length 28 cm, diameter 6 cm, sensitive area of impact plate 1 cm^2. Ions originated on the impact plate at the center, and at radii of 0.2, 0.4, and 0.55 cm. Groups of 500 ions at each location were defined to have mass of 100 amu, initial kinetic energy of 25 ± 15 eV, and a *cos* θ angular distribution about the normal. Figure 4.19 shows typical simulated ion trajectories under these conditions. Figure 4.20 shows an enlargement of ions with m/z 200 and 201 as they approach the detector. Mass resolution ($m/\Delta m$) of simulated ions was 350-400, sufficient to resolve isotopes of any element. Resolution was not reduced for ions originating away from the center of the impact plate, although the number of ions reaching the detector was reduced. Including a slight curvature to the impact plate improved this situation in simulations. For most simulations 10-15% of ions reached the detector, assuming 70% transmission for the extraction grid and 95% transmission for all other grids. Narrowing the ring aperture such that 5% of ions reached the detector resulted in a simulated mass resolution of around 600. The results of these simulations are consistent with observations using hypervelocity microparticle impacts on the energy analyzer.

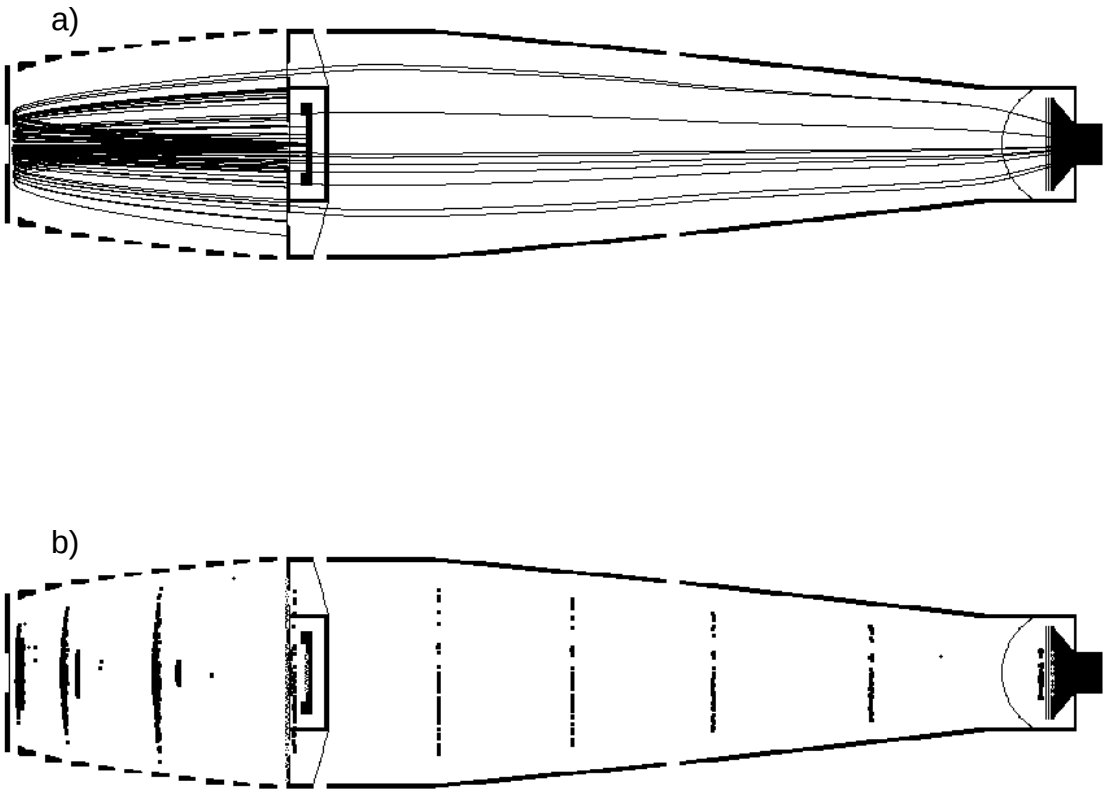

Figure 4.19. Simulated ion trajectories on proposed instrument. Diagram b) shows locations of ions at time intervals of 0.4 μs.

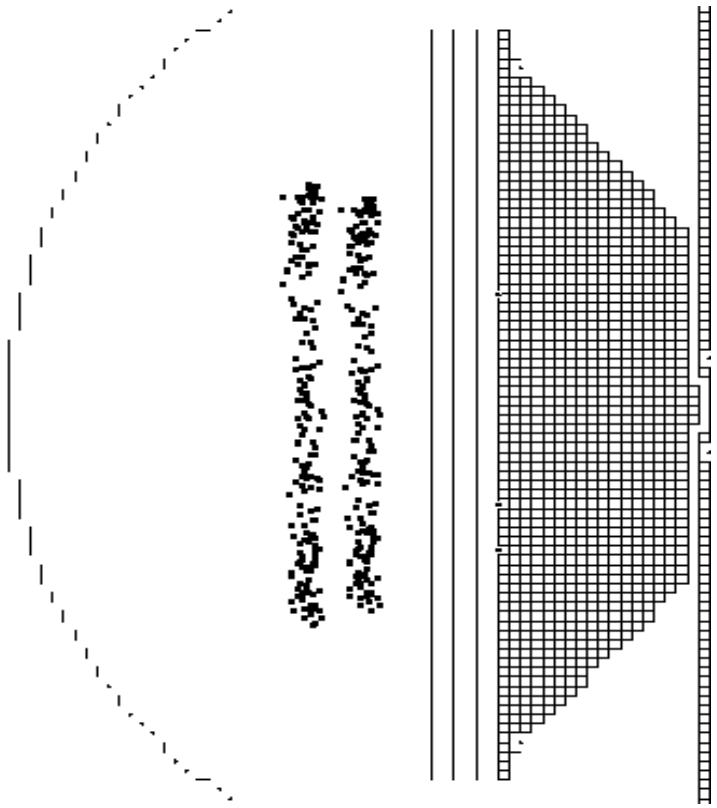

Figure 4.20. Ions of mass 200 and 201 reaching the detector of the high-flux dust analyzer.

References

1. Fair, H., *Hypervelocity then and now.* Int J Impact Engng, 1987. **5**: p. 1-11.
2. Shelton, H.; Hendricks, C. D., Jr.; Wuerker, R. F., *Electrostatic acceleration of microparticles to hypervelocities.* J Appl. Phys., 1960. **31**(7): p. 1243-1246.
3. Friichtenicht, J. F., *Two-million-volt electrostatic accelerator for hypervelocity research.* Review of Scientific Instruments, 1962. **33**(2): p. 209-212.
4. Shibata, H.; Kobayashi, K.; Iwai, T.; Hamabe, Y.; Sasaki, S.; Hasegawa, S.; Yano, H.; Fujiwara, A.; Ohashi, H.; Kawamura, T.; Nogami, K.-i., *Microparticle acceleration by a van de Graaff accelerator and application to space and material sciences.* Radiation Physics and Chemistry, 2001. **60**: p. 277-282.
5. Friichtenicht, J. F., *Micrometeoroid simulation using nuclear accelerator techniques.* Nuclear Instruments and Methods, 1964. **28**: p. 70-78.
6. Auer, S. and Sitte, K., *Detection technique for micrometeoroids using impact ionization.* Earth and Planetary Science Letters, 1968. **4**: p. 178-183.
7. Hansen, D. O., *Mass analysis of ions produced by hypervelocity impact.* Applied Physics Letters, 1968. **13**(3): p. 89-91.
8. Friichtenicht, J. F.; Roy, N. L.; Becker, D. G. *The Cosmic Dust Analyzer: experimental evaluation of an impact ionization model*. in *International Astronomical Union Colloquium #13*. 1971. State University of New York, Albany, NY: Scientific and Technical Information Office, NASA, Washington, D.C.
9. Dietzel, H.; Neukum, G.; Rauser, P., *Micrometeroid simulation studies on metal targets.* Journal of Geophysical Research, 1972. **77**(8): p. 1375-1395.
10. Roy, N. L., *Research Investigations of the Physical Interactions and Phenomena Associated with Hypervelocity Sub-micron Particles*. 1975, TRW Systems Group: Redondo Beach, CA. p. 67.
11. Sutton, G. W. and Sherman, A., *Engineering Magnetohydrodynamics*. 1965, New York: McGraw Hill.

12. Perkins, M. A.; Simpson, J. A.; Tuzzolino, A. J., *A cometary and interplanetary dust experiment on the Vega spacecraft missions to Halley's Comet.* Nuclear Instruments & Methods in Physics Research, Section A: Accelerators, Spectrometers, Detectors, and Associated Equipment, 1985. **239**: p. 310-323.

13. Kissel, J. and Krueger, F. R., *Ion formation by impact of fast dust particles and comparison with related techniques.* Applied Physics A: Solids and Surfaces, 1987. **42**: p. 69-85.

14. Kissel, J. and Kreuger, F., *Time-of-flight mass spectrometric analysis of ion formation in hypervelocity impact of organic polymer microspheres: comparison with secondary ion mass spectrometry, 252Cf mass spectrometry and laser mass spectrometry.* Rapid Communications in Mass Spectrometry, 2001. **15**: p. 1713-1718.

15. Kissel, J.; Sagdeev, R. Z.; Bertaux, J. L.; Angarov, V. N.; Audouze, J.; Blamont, J. E.; Buchler, K.; Evlanov, E. N.; Fechtig, H.; Fomenkova, M. N.; von Hoerner, H.; Inogamov, N. A.; Khromov, V. N.; Knabe, W.; Krueger, F. R.; Langevin, Y.; Leonas, V. B.; Levasseur-Regourd, A. C.; Managadze, G. G.; Podkolzin, S. N.; Shapiro, V. D.; Tabaldyev, S. R.; Zubkov, B. V., *Composition of Comet Halley dust particles from Vega observations.* Nature (London), 1986. **321**: p. 280-282.

16. Kissel, J.; Brownlee, D. E.; Buchler, K.; Clark, B.; Fechtig, H.; Grun, E.; Hornung, K.; Igenbergs, E. B.; Jessberger, E. K.; Kreuger, F.; Kuczera, H.; McDonnell, J. A. M.; Morfill, G. E.; Rahe, J.; Schwehm, G.; Sekanina, Z.; Utterback, N. G.; Volk, H. J.; Zook, H. A., *Composition of Comet Halley particles from Giotto observations.* Nature (London), 1986. **321**: p. 336-337.

17. Lawler, M. E.; Brownlee, D. E.; Temple, S.; Wheelock, M. M., *Iron, magnesium, and silicon in dust from comet Halley.* Icarus, 1989. **80**: p. 225-242.

18. Kissel, J. and Krueger, F. R., *Mass-spectrometric in situ studies of cometary organics for P/Halley and options for the future.* Advances in Space Research, 1995. **15**(3): p. (3)59-(3)63.

19. Kissel, J. and Kreuger, F. R., *The organic component in dust from Comet Halley as measured by the PUMA mass spectrometer o board Vega 1.* Nature (London), 1987. **326**: p. 755-760.

20. Hornung, K. and Kissel, J., *On shock wave impact ionization of dust particles.* Astronomy and Astrophysics, 1994. **291**: p. 324-336.

21. Hornung, K.; Malama, Y. G.; Thoma, K., *Modeling of the very high velocity impact process with respect to in situ ionization measurements.* Advances in Space Research, 1996. **17**(12): p. (12)77-(12)86.

22. Hornung, K.; Malama, Y. G.; Kestenboim, K. S., *Impact vaporization and ionization of cosmic dust particles.* Astrophysics and Space Science, 2000. **274**: p. 355-363.

23. Krueger, F. R., *Ion formation by high- and medium-velocity dust impacts from laboratory measurements and Halley results.* Advances in Space Research, 1996. **17**(12): p. (12)71-(12)75.

24. Abramov, V. I.; Bandura, D. R.; Ivanov, V. P.; Sysoev, A. A., *Energy and angular characteristics of ions emitted in the impact of accelerated dust particles on a target.* Sov. Tech. Phys. Lett., 1991. **17**(3): p. 194-195.

25. Ratcliff, P. R.; Reber, M.; Cole, M. J.; Murphy, T. W.; Tsembelis, K., *Velocity thresholds for impact plasma production.* Advances in Space Research, 1997. **20**(8): p. 1471-1476.

26. Ratcliff, P. R. and Allahdadi, F., *Characteristics of the plasma from a 94 km/s microparticle impact.* Advances in Space Research, 1996. **17**(12): p. (12)87-(12)91.

27. Novikov, L. S.; Semkin, N. D.; Kulikauskas, V. S.; Semenchuk, S. M.; Kiryukhin, V. P., *Mass spectrometry of ions emitted in collisions of accelerated dust particles with target.* Sov. Phys. Tech. Phys., 1988. **33**(6): p. 680-682.

28. Sysoev, A. A.; Bandura, D. R.; Ivanov, V. P., *Mechanism of ionization in a low-velocity collision of charged microparticles.* Sov. Tech. Phys. Lett., 1992. **18**(8): p. 486-488.

29. Sysoev, A. A.; Ivanov, V. P.; Barinova (Komova), T. V.; Surkov, Y. A., *Mass spectra formation from charged microparticles.* Nuclear Instruments & Methods in Physics Research, Section B: Beam Interactions with Materials and Atoms, 1997. **122**: p. 79-83.

30. McDonnell, J. A. M.; Aguti, E. D.; Willis, M. J. *Pre-contact microdischarge from charged particulates*. in *Proceedings of the 7th Spacecraft Charging Technology Conference, 23-27 April 2001*. 2001. Noordwijk, The Netherlands: European Space Agency.

31. Simpson, J. A., *Design of retarding field energy analyzers.* Rev. Sci. Instrum., 1961. **32**(12): p. 1283-1293.

32. Roberts, R. H., *Design details for a small cylindrical mirror analyzer.* Journal of Physics E: Scientific Instruments, 1982. **15**: p. 382-385.

33. Stenzel, R. L.; Williams, R.; Agüero, R.; Kitazaki, K. L., A; McDonald, T.; Spitzer, J., *Novel directional ion energy analyzer.* Review of Scientific Instruments, 1982. **53**(7): p. 1027-1031.

34. Kang, H. and Beauchamp, J. L., *Pulsed laser evaporation and ionization of solid metal targets. Implications for studying the gas-phase reactions of laser-generated atoms and ions.* Journal of Physical Chemistry, 1985. **89**: p. 3364-3367.

35. Cotter, R. J., *Time-of-flight Mass Spectrometry*. 1997, Washington, D. C.: American Chemical Society. 326.

36. Jyoti, G.; Gupta, S. C.; Ahrens, T. J.; Kossakovski, D.; Beauchamp, J. L., *Mass spectrometer calibration of high velocity impact ionization based cosmic dust analyzer.* International Journal of Impact Engineering, 1999. **23**: p. 401-408.

37. Jyoti, G.; Gupta, S. C.; Ahrens, T. J.; Kossakovski, D.; Beauchamp, J. L., eds. *Mass spectrometer calibration of cosmic dust analyzer*. Shock Compression of Condensed Matter, ed. Furnish, M. D.; Chhabildas, L. C.; Hixson, R. S. 1999, American Institute of Physics.

38. Odom, R. W. and Schueler, B., *Laser Microprobe Mass Spectrometry: Ion and Neutral Analysis*, in *Lasers and Mass Spectrometry*, Lubman, D. M., Editor. 1990, Oxford University Press: New York. p. 103-137.

39. Giudicotti, L.; Bassan, M.; Pasqualotto, R.; Sardella, A., *Simple analytical model of gain saturation in microchannel plate devices.* Rev. Sci. Instrum., 1993. **65**(1): p. 247-258.

40. Maechling, C. R.; Clemett, S. J.; Zare, R. N., *13C/12C ratio measurements of aromatic molecules using photoionization with TOF mass spectrometry.* Chemical Physics Letters, 1995. **241**: p. 301-310.

41. Kimura, H. and Mann, I., *The electric charging of interstellar dust in the solar system and consequences for its dynamics.* Astrophysical Journal, 1998. **499**(454-462).

42. Burchell, M. J.; Cole, M. J.; McDonnell, J. A. M., *Role of particle charge in impact ionization by charged microparticles.* Nuclear Instruments & Methods in Physics Research, Section B: Beam Interactions with Materials and Atoms, 1998. **143**: p. 311-318.

43. Agutti, E. D., *Charged Particles in GEO: The Role of Electrostatic Charge in Particulate Impacts on the GORID Dust Detector*. 1999, Masters Thesis, University of Kent, Canterbury.

44. Ray, R. and Mahan, G. D., *Dynamical image charge theory.* Physics Letters A, 1972. **42A**(4): p. 301-302.

45. Sahni, V. and Bohnen, K.-P., *Image charge at a metal surface.* Physical Review B, 1985. **31**(12): p. 7651-7661.

46. Eyges, L., *The Classical Electromagnetic Field*. 1972, New York: Dover.

47. Setterland, C. J. and Barany, A., *Theoretical study of image charge acceleration of highly charged ions in front of a metal surface.* Nuclear Instruments & Methods in Physics Research, Section B: Beam Interactions with Materials and Atoms, 1995. **98**: p. 407-409.

48. Kasperovich, V.; Wong, K.; Tikhonov, G.; Kresin, V. V., *Electron capture by the image charge of a metal nanoparticle.* Physical Review Letters, 2000. **85**(13): p. 2729-2732.

49. Jung, Y.-D., *Image charge effects on electron capture by dust grains in dusty plasmas.* Physical Review E, 2001. **64**: p. 017401.

50. Dahl, D. A., *SIMION 3D*. 2000, Idaho National Engineering and Environmental Laboratory: Idaho Falls, ID.

51. Jung, Y.-D., *Image charge effects on bremsstrahlung radiation from electron-dust grain scatterings in dusty plasmas.* Physics of Plasmas, 1999. **6**(8): p. 3396-3399.

52. Andersson, P. U. and Pettersson, J. B. C., *Ionization of water clusters by collisions with graphite surfaces.* Zeitschrift fur Physik D, 1997. **41**: p. 57-62.

53. Matthew, M. W.; Buehler, R. J.; Ledbetter, M.; Friedman, L., L*arge, energetic cluster impacts on surfaces.* Nuclear Instruments & Methods in Physics Research, Section B: Beam Interactions with Materials and Atoms, 1986. **14**: p. 448-460.

54. Andersson, P. U. and Pettersson, J. B. C., *Water cluster collisions with graphite surfaces: angular-resolved emission of large cluster ions.* Journal of Physical Chemistry, 1998. **102**: p. 7428-7433.

55. Fabris, D.; Wu, Z.; Fenselau, C. C., *Massive cluster impact ionization on a four sector tandem mass spectrometer.* Journal of Mass Spectrometry, 1995. **30**: p. 140-143.

56. Mahoney, J. F.; Perel, J.; Ruatta, S. A.; Martino, P. A.; Husain, S.; Lee, T. D., Rapid Communications in Mass Spectrometry, 1991. **5**: p. 441.

57. Aksyonov, S. and Williams, P., *Impact desolvation of electrosprayed microdroplets - a new ionization method for mass spectrometry of large biomolecules.* Rapid Communications in Mass Spectrometry, 2001. **15**(21): p. 2001-2006.

58. Berglund, R. N. and Liu, B. Y. H., *Generation of monodisperse aerosol standards.* Environmental Science and Technology, 1973. **7**(2): p. 147-153.

59. Savart, Annales de Chimie (Paris), 1833. **t. liii**.

60. Rayleigh, L., Proceedings of the Royal Society of London, 1879. **29**: p. 71.

61. Rayleigh, L., Proceedings of the London Mathematical Society, 1878. **10**: p. 4.

62. Ratcliff, P. R.; McDonnell, J. A. M.; Firth, J. G.; Grun, E., *The Cosmic Dust Analyzer.* J. British Interplanetary Soc., 1992. **45**(9): p. 375-380.

63. Austin, D. E.; Ahrens, T. J.; Beauchamp, J. L., *Dustbuster: a compact impact-ionization time-of-flight mass spectrometer for in situ analysis of cosmic dust.* Review of Scientific Instruments, 2002. **73**(1): p. 185-189.